REPUBLIC OF TÜRKİYE

ALTINBAŞ UNIVERSITY

Institute of Graduate Studies

Electrical and Computer Engineering

BLOOD GLUCOSE MICROWAVE SENSOR BASED OPTICALLY CONTROL DETECTION

Maryam Sami ALMEHMES

Master's Thesis

Supervisor

Asst. Prof. Dr. Mesut ÇEVİK

Istanbul, 2022

BLOOD GLUCOSE MICROWAVE SENSOR BASED OPTICALLY CONTROL DETECTION

Mryam Sami ALMEHMES

Electrical and Computer Engineering

Master's Thesis

ALTINBAŞ UNIVERSITY

2022

The thesis titled BLOOD GLUCOSE MICROWAVE SENSOR BASED OPTICALLY CONTROL DETECTION prepared by MARYAM SAMI MAJEED ALMEHMES and submitted on 22/12/2022 has been **accepted unanimously** for the degree of Master of Science in Electrical and Computer Engineering.

____

Asst. Prof. Dr. Mesut ÇEVİK

The Supervisor

Thesis Defence Committee commission:

Asst. Prof. Dr. Mesut ÇEVİK	Department of Electrical and Electronics Engineering, Altinbaş University	___________________
Asst. Prof. Dr. Hasan ABDULKADER	Department of Computer Engineering, Altinbaş University	___________________
Asst. Prof. Dr. N.Ozlem UNVERDI	Department of Electronica and Communication Engineering, Altinbaş University	___________________

I hereby declare that this thesis meets all format and submission requirements of a MASTER'S thesis.
Submission date of the thesis to Institute of Graduate Studies: 2022/12/___

I hereby declare that all information/data presented in this graduation project has been obtained in full accordance with academic rules and ethical conduct. I also declare all unoriginal materials and conclusions have been cited in the text and all references mentioned in the Reference List have been cited in the text, and vice versa as required by the abovementioned rules and conduct.

Maryam Sami ALMEHMES

Signature

DEDICATION

First and foremost, I pray to God Almighty for the wisdom, health, strength, _knowledge, and guiding abilities essential to conclude my research. The thesis is honestl dedicated to my parents, who served as my motivation and who always reminded me that every accomplishment in my life is a gift to them. I want to specifically thank my supervisor, Asst. Prof. Mesut EVK, for all the assistance he provided me with my studies.

PREFACE

The auther would like to thank Taha A. Elwi for his unwavering support and the International Applied and Theoretical Research Centre (IATRC), Baghdad Quarter, Iraq for their assistance during the measuring procedure.

ABSTRACT

BLOOD GLUCOSE MICROWAVE SENSOR BASED OPTICALLY CONTROL DETECTION

Almehmes, Maryam Sami Majeed

M.Sc, Electrical And Computer Engineering, Altınbaş University,

Supervisor: Asst. Pros. Dr. Mesut ÇEVİK

Date: 12/2022

Pages:74

The development of a microwave resonator design for noninvasive blood glucose biological sensing is the focus of this thesis. The proposed sensor is built upon a printed transmission line with a characteristic impedance of 50. The diffusion-lines have been overtaken by a sweep penny elegance chaotic' meander line. The construction is divided into two symmetric pieces, which are joined to one another by a resistor that changes in resistance in response to light (LDR). In order to increase the field fringing through the sample being examined, an interdigital capacitor is inserted in parallel with the meander line configuration. It is discovered that the proposed sensor offers numerous frequency resonances. The authors used frequency resonance at 3.46GHz to ensure that the detection would work effectively with fluctuating blood glucose levels. In order to comprehend the effects of altering the blood glucose level on the transmission loss spectra of the proposed sensor, which are measured in terms of S11 magnitude, the proposed sensor is developed and experimentally tested with 100 patients at the international/Applied &Theoretical/Research-Center (IATRC). The performance of the suggested sensor is evaluated and enhanced using circuit model theory. Lastly, the finite integral approach algorithm in the commercial software program Computer/Simulation/Technology of Micro/Wave/Studio is used to numerically validate the design performance (CSTMWS). In the end, encouraging experimental and theoretical discoveries are made.

Keywords: LDR, Meander, Glucose Sensor, Microwave Resonator, IATRC.

TABLE OF CONTENTS

Pages

ABSTRACT……………………………………………………………………...………..…...vii

LIST OF TABLES...………………………………………………………………..……....x

LIST OF FIGURES……………………..……..…………………………………………...xi

ABBREVIATIONS...…………………………………...…………………………….....xii

LIST OF SYMBOLS……………………………………………………….……...…....xv

1. INTRODUCTION……..…………………...……………………...…..……….……..1

1.1 OVERVIEW……………………………………………………………….………………..1

1.2 MOTIVATIONS…………..…………………………………………...….. ……..……...2

1.3 LITERATURE SURVEY….….............……….…………………………..…................6

1.4 AIM OF THE THESIS……………….…….…………………….…..……....................... 14

1.5 THESIS OUTLINE………......................…………………..……………………...... 14

2. THEORETICAL BACKGROUND…...…....…………………………………...…..... 15

2.1 OUTLINE……………...…………………………………...…................................... 15

2.2 OVERVIEW OF RF/MICROWAVE RESONATORS………................................. 15

2.3 MICROSTRIP FILTER….……………………….……………….................................... 20

2.3.1 Effective Dielectric Constant Characteristic Impedance and Attenuation..................20

2.4 DISCONTINUITIES IN MICROSTRIP ELEMENTS…………..……………………… 21

2.4.1 Open-End Circuit……………………………………………….……………..………….21

2.4.2 Steps……………………....…………………………………………..……….….... 21

2.4.3 Gaps…………………….....……………………...……..……………….……...... 23

2.4.4 Right Angle Bends………….…………….………………..……………..…...23

2.5 MICROSTRIP RESONATORS … ……………………………………..…............... 24

2.5.1 Stepped-Impedance Resonator(SIR)………..…………………….……...…… …24

2.5.2 Square-Loop Ring Resonator…………………………..…...………….……….....24

2.5.3 Meandered Resonator……….………………………………………....………...... 25

2.5.4 Substrate-Integrated Waveguide(SIW) Resonator………………..………...… …..25

2.6 COUPLING TYPES FOR TRANSMISSIOM LINES………………….……….…... 26

2.6.1 Electric Coupling………………...27
2.6.2 Magnetic Coupling……………..29
2.6.3 Mixed Coupling…………………………..30
2.7 COUPLING MICROSTRIP LINES………………….................................31
2.7.1 Even Odd Mode Capacitance……………………………………........31
2.7.2 Even Odd Styles…...33
2.8 MICROWAV FILTER NETWORK VARIABLES AND PARAMETERS………..33
2.8.1 Scattering Parameter…………………………………………………..……34
2.8.2 Filter Bandwidth and Fractional Bandwidth…………………………..………..35
3. DISCUSSION OF THE METHODOLOGY……………………………..…………….41
3.1 INTRODUCTION……………………..…………………..……………………….41
3.2 SENSOR DESIGN AND DETAILS……………………………………...…….....46
3.3 DESIGN METHODOLOGY BASED CIRCUIT ANALYSIS………....................49
4. SENSING METHODOLOGY AND NUMEICAL RESULTS……………....……....53
4.1 SENSOR OPERATION AND RECONFIGURATION PROCESS ……………...…..55
4.2 EXPERIMENTAL VALIDATIONS ……….………………………….................56
5. CONCLUSION AND FUTURE WORKS………………….………………………..59
5.1 CONCLUSION…….………..……………………………………...….……..59
5.2 FUTURE WORKS…..………………………………………………….……....59
REFERENCES…….………………………...………………………..…..……………...…61

LIST OF TABLES

Pages

Table 2.1: Performance analysis of microstrip antennas……..………………..…………..…39

Table3.1: Lumped element values of the equivalent circuit model in fig3.6…………………....52

Table4.1: Measured glucose influence on the proposed sensor performance…………………..…..58

LIST OF FIGURES

Pages

Figure 2.1: General microstrip structure…………..……………………………….…………18
Figure 2.2: Fields distributions……..……..……………………………………………..…19
Figure 2.3: Filter attenuation characteristic……………..………………………………………19
Figure 2.4: Micro strip discontinuities…...………..……………………………………......…...22
Figure 2.5: Schematic of the Stepped-impedance resonator………..…………………….…..…...24
Figure 2-6: General structure of the square-loop ring resonator……………………..…...……..25
Figure 2.7: 2-D Meandered and 2-D Hilbert microstrip resonators with the same length and spacing……………………………………………………………………………………...…25
Figure 2.8: Scheme of SIW with air holes and metallic vias….………..…………….....…...…..26
Figure 2.9: Transmission lines coupling schemes………………………………………………27
Figure 2.10: Electric coupling………...………………….……………………..…………..28
Figure 2.11: Magnetic coupling………..……………………………………...…………...29
Figure 2.12: Mixed coupling limped element……………....……………………...…………..30
Figure 2.13: Cross-section of coupled microstrip lines…..……………………………………..31
Figure 2.14: TEM modes for a pair of coupled lines……..……………………………….……….32
Figure 2.15: Two-port network……..………………………………..…………………......34
Figure 2.16: Performance analysis of microstrip antennas…,,………………..…………......….40
Figure 3.1: The proposed sensor geometry………..……………..…………………………..……48
Figure 3.2: The proposed CSI structure……..………………………………………….……………49
Figure 3.3: The proposed IDC structure….………..…………………………………….…………50
Figure 3.4: The proposed Hilbert structure…………………..…………………………….……………51
Figure 3.5: The proposed circuit model of the proposed back loop structure…….….…………51
Figure 3.6:Theproposedcircuitmodeloftheproposedsensorstructure………..……..…………….52
Figure4.1:The simplified block diagram of the design based on reconfigurable technology…..….……………………...…………………………………………………………....53
Figure 4.2:EvaluatedS21spectrawithrespecttovaryingtheLDRvalue...….……...………………..56
Figure 4.3: Experimental part………………..……..………………………...……………………..57

ABBREVIATIONS

LDR	: Light Depended Resistor
LATRC	: International Applied and Theoretical Research Canter
CST MWS	: Computer Simulation Technology of Micro Wave Studio
LR	: Return Loss
OFDM	: Orthogonal Frequency Division Multiplexing
IL	: Insertion Loss
UWB	: Ultra Wide Bandwidth
WCE	: Wireless Capsule Endoscope
EH	: Energy Harvesting
AP	: Access Point
MVs	: Mobile Users
FD	: Full Duplex
HD	: Half Duplex Mode
UL	: Up Link
DL	: Downlink
BAN	: Body Area Network
HFSS	: High Frequency Structure Simulator
SIR	: Stepped Impedance Resonator
UWB	: Wideband Millimeter Wave Pass
QMR	: Quintuple Mode Resonator

TWB	: Triple Wideband Filter
MMR	: Multi Mode Resonator
GPS	: Global Positioning System
MUT	: Material Under Test
IDC	: Inter digital Capacitor
OSM	: Open Stub Inverted Meander Line
MIMO	: Multiple Input Multiple Output
ADMM	: Alternating Direction Method Of Multiplies
OOBE	: Out of Band Emission
CI	: Close-In
MPA	: Massage Passing Algorithm
FH	: High-Band Frequencies
FL	: Lower-Band Frequencies
FBW	: Fractional Bandwidth
FDA	: Frequency Diversity Array
WET	: Wireless Energy Transfer
USRPs	: Universal Software Radio Peripherals
PLS	: Physical Layer Security
SUT	: Sample Under Test
CST	: Computer Simulation Technology
2D	: Two Dimensions

AFM : Atomic Force Microscopy

LIST OF SYMBOLS

μ : Electron Mobility

λ : Wavelength

ω : Angular Frequency

σ : Conductivity

v : Relaxation Frequency

e : Electron Charge

Fc,v : Fermi Distribution

Es : Low Frequency Permittivity

ω0 : Angular Frequency Resonance

γ : Damping Factor of Oscillation

ωD : Plasma Resonance Frequency

ωτ : Collision Frequency

aoȣai : Outer and Inner Radii

ηr : Efficiency of radiation

l : Electrical Length

THz : Tera Hertz

G : Matching gap

D : Directivity

Λo : Free Space Wavelength

E : Electric Field

H : Magnetic Field

Σ : Conductivity

B : Propagation constant

Φ : Azimuth Angle

Ω : Ohm Resistor

A : Attenuation Constant

Δ : Surface Losses

Δq : Variation Change

INTRODUCTION

1.1 OVERIEW

In biomedical applications recently, microwave sensors have multi-functional importance including: nondestructive without invasion sensing process to characterize bio-dielectric properties [1]. Biomedical engineering has recently moved towards combining personalized therapy to provide combinations of diagnosis and treatment for individuals [2]. These systems have major goals, such as developing a customized plan for each patient based on microwave technologies such as microwave-resonator-sensors [3]. The most important advantage of microwave energy is the ability to penetrate non-destructively into the human tissues with nonionizing effects [4]. Nevertheless, microwave technology can provide an accurate diagnosis with a quick response [5]. Microwave biomedical sensors must provide high sensitivity with low energy [6]. This is due to the fact the inherent properties of the biological fluids, such as spinal, blood, and urine, are composites of water, salts, glucose, etc. [7]; that could be harshly affected by high radiative energies with long use [8]. Therefore, a chance of isolating ionizes could take place with time, which realizes difficult acquisition and association [9].

It is important to mention that, lifestyle is not always consistent, due to developing chronic diseases; which is considered a global health problem [10]. Therefore, the health care system requires a continuous update to be computable with the new generations of diseases [11]. Researchers, in this field, face a major challenge, which is developing modern biomedical systems with low cost [12]. This is achieved by detecting medical problems and diseases in the early stages through using personal wearable and/or planted sensors [13]. Modern communication technologies such as (smartphones) have been widely integrated with personal healthcare systems [14]. Such integration demonstrates a bonier type of electronic health monitoring that is still effective solution for many biomedical research interests [15]. Therefore, the electronic health systems provide long evolution care without continuous personal physician doctor observation for essential medical control and identification [16]. Consequently, microwave sensors are considered good candidates for biomedical applications [17]; they have been developed by researchers to be alternatives to invective traditional methods [18]. The property that determines electromagnetic fields that interact with materials depends on their molecular structure a basic principle on which biosensors of electromagnetic devices depend [19]. So, biological tissues can be inspected by scrutinizing the diverseness of their insulating properties in response to the activity applied [20].

Microwave energy has several advantages such as the ability of penetration in the biological media to carry out non-invasive measurements [21]. Moreover, microwaves constitute nonionizing fields, so will keep away from threats linked to the adoption of another model of radiation, such as x-rays [22]. Biological atoms are polarized similar to water when exploring microwave fields [23], and the excitation wave is seen quietly traveling to an average free-space [24]. The speed of wave propagation in biological environments is considered to be a change, as the microwave biosensor aims to change these changes into a quantifiable signal that gives a variety of specific biological parameters [25].

1.2 MOTIVATIONS

Filters drama an important-role in any type of microwave systems. The typical function of filters is to let in the desired frequencies while rejecting the undesirable ones. Multiband operation is the most desired circuitry due to their capacity of adaptation in different communication environments [7]. In order to operate at one, two, or more frequency bands, high performance electronic circuitries are compacted with microwave filters [5].

In wireless communications systems, RF microwave filters can be used in cellular phones, radars, satellites, and remote sensing, transmitters, and receivers. The filter should have low input return loss (LR), S_{11}, and high insertion loss (IL), high-frequency selectivity, compression, and low cost to obtain optimum filter performance. Microwave and millimeter-wave technology could coexist together for future wireless communications, to perform multi-band operations to provide essential coverage for short-range communications with high data transfer rates [8]. The most widely used in microwave filter design are microwave filters based on fine lines for their benefits such as little charge, small size, and comfort of manufacture [9]. To manufacture multi-band filters, many technologies have been used such as micro-resistance, gradient resonators, multi-mode resonators, and parallel line resonators. And design by inserting transmission zeros [7]. To decrease complexity and increase sensor compactness, a graded resistance resonator for two or more transmission lines with a high characteristic impedance can be employed. This work demonstrates the scheme for operating multiband microwave filter design for operating in microwave frequencies for biomedical sensor applications.

Sixth-generation (6G) mobile communications networks are an example of future wireless technologies.are predicted to be able to transmit data at previously unheard-of speeds thanks to little terahertz (Low-THz-bands, 100Ghz/bands-to-1.0THz/bands) technology. Transmission rates and channel/capacity can be maintained by boosting carriers from millimeter wave to THz. Very high gain antennas are required to overcome the Low-THz source's power limitation and compensate for the significant broadcast loss of Low-THzwaves in free areas. Lately, additive solenoid manufacturing and r-axis mounting technologies have made it easier and less expensive to build antennas with complex configurations. As a first step, this paper presents many state-of-the-art techniques for low-THz and submillimeter wave antenna development. The outcomes of latest high-gain broadband probes are set, too. Below is a comparison of several previously reported antennas. Using the Fabry-Perot nook concept, it simulates a high-gain 300GHz broadband probe. Future THz applications may use a synthetic FPC probe made using AM equipment that is both affordable and very reliable. The performance of an antenna in the small/THz band depends heavily on how precisely it is built. These techniques could need a lot of time and money to produce standard THz devices. Here, wideband Low-THz antennas, their manufacturing processes, and the many techniques researchers have employed to boost the antenna's gain are discussed.It is possible to build a 300GHz three-switched beam antenna utilizing these two antennas [1]–[5].

To verify the recommended antenna's performance, a 30 GHz scaled antenna element was constructed using the MBJ method, which is noticeably quicker and less expensive than the previous production methodology. A simulated and measured test's results could be agreed upon. Comparisons of the different types, sizes, frequency ranges, and processing techniques are displayed. Our antenna is the first in the mm-wave frequency to produce high-gain, multi-beam radiation with a straightforward all-metal structure thanks to the use of AM methods. The components created for this inquiry were determined to have a high degree of dimensional correctness. We might soon be able to use AM accuracy improvements to leverage Our Low-THz antennas were made using cutting-edge printing techniques including hybrid 3DP and 4D printing. Phased array systems with low-THz active circuits that mix active and passive circuits on a single chip represent the next stage of our research. We'll delve deeper into our study of low-frequency scanning antennas. It uses a short-range (IR) ultra-wide-bandwidth (UWB) spread-spectrum (UWB) communication technique. This research presents and evaluates for the wireless capsule endoscope (WCE) communication system, an unique antenna design . Three frequency bands are included in the antenna design (38.5, 48.2, and 57.2 MHz operating frequencies). Three transmitting antennas are mounted on the body for the antenna performance test. A muscle equivalent phantom can be used to replicate the specific echo and broadcast numbers, electric/-magnetic/ground distributions, and absorption rates (S/A/R). Using a battery-powered IR transceiver, the performance of transmission in a liquid phantom is also examined. Hence, utilizing the suggested antenna, individual WCE pictures may be received less than 50mm-90mm from the antenna at a total data rate of 3.75Mbps-2.5Mbps. Attenuation at 50mm is 32dB-52dB at 38.5MHz-55.6MHz. Three single-group in-figure conveyance probes for the WCE message scheme indicating response were created and evaluated in this work, along with the message presentation. Low frequency multiband communications attenuated to 50 MHz, 403.5 MHz, and 2400 MHz, respectively were tested using a 50-mm muscle phantom. To make sure their probe imitation model was realistic, the scientists created Rx and Tx3 prototypes and carried out free space reflection experiments. They next performed simulations to determine whether their findings would be affected by variations in resonance frequency, reflection coefficients, and transmission coefficients. [6]-[10]. The Rx array's improvement of the transmission coefficient in the presence of misalignment and its effects. The transmission coefficient augmentation by the Rx array under the misalignment scenario and its implications on the SAR and maximum safe input power are some of the subjects explored in this paper. Coupling occurred at roughly the anticipated frequency of 576 MHz, aside from the VNA's validation of the antenna reflection and transmission coefficients. The battery-operated IR transceiver's transmission quality was evaluated last. Contrary to models, when the transmitting antenna frequency is altered, Increases in transmission attenuation of 10.3, 13.3, and 16.4 dB occur. Medical imaging applications typically use data speeds of 3.75 Mbps and 2.5 Mbps at 50 mm and 90 mm, respectively. [11]–[15]. An IoT network's nodes can each power autonomous wireless communication systems with renewable energy sources like energy production (EH). In this work, WPCN protocols for everyday communication are examined. entre un punto de acceso (AP) and a significant portion of smartphone users (MUs). Several antennas are used by the AP's full-duplex (FD) capabilities. A MU only has one antenna, the only half-duplex means of communication available to it (HD). There are two types of MUs connected to the FD-AP: uplink (UL) and downlink (DL), which have different time allocation and channel access policies. To increase the UL weighted sum rate, channel allocations, time constraints, and power resources are analyzed and modified. The optimization issue for addition rate is not convex. Iteratively improving the UL slanted quantity rates for the FD-WPCN classification. HD-WPCN statement After these changes have been made, there is currently availability among the AP and several MUs. In various simulations, the HD-WPCN method is contrasted with our FD-WPCN strategy. In the tiny AP convey SNR range, modeling results indicate that FD-WPCN appears to perform better than HD-WPCN. Due to an increase in FD-AP self-meddling, high AP transmit SNR results in the opposite behavior. In this study, researchers created a completely new type of antenna. In UWB frequency kind of 3.75GHz-4.25GHz, the antenna is used for IEEE802.15.6BAN. The antenna measures 89mm in length, 60mm in width, and 21mm in height. The antenna has an 8dBi gain at the primary frequency of 4 GHz. To evaluate the antenna behavior near the hominid figure, particularly the small intestine, wireless capsule endoscopy localization is required. A tissue-layer classical, which replicates the dielectric faces of real bulk tissues, was used to model the dielectric properties of humanoid figure matters at 4GHz. After that, research on voxel replicas was carried out. After comparing the intrinsic qualities of the body to those of the antenna, the power flow propagation into tissues was examined. The antenna communication of a pill that has been administered into the small intestine is examined using these methods. The aerial's accuracy for free-planetary broadcast was then evaluated. These findings warrant a physical examination of both male and female patients. The fake fallouts were generated by CST Microwave Studio. The findings were supported by measurements taken in an anechoic chamber at the University of Oulu. Frequency readings were transformed into time measurements through post-processing. As a result, there is agreement between models and measurements. UWB signaling compliant with IEEE 802.15.6 could be used to produce antennas for wireless capsule endoscopic communications. This research introduces a novel antenna design.[16]-[20].

1.3 LITERATURE SURVEY

The rapid development of microwave sensor technologies has increased dramatically. Thus, it leads to the requirement of designing novel resonators to operate at different frequencies at the same time. There are many techniques used to design a multi-band resonator, a cut-off resonator, a quarter-step impedance resonator, a built-in resonator, the winding split–ring resonator, and the substrate integrate waveguide resonator. Here, we will explain the methods and results obtained by the researchers.

In 2012 Feng et al:

A multi- mode resonator for WLAN applications was used create a two-band pass sifter using the anosoft HFSS simulator. By altering the characteristic impedance and the four odd/even modes of the multimode resonator, the bandwidth of the generated passbands can be altered. The two passbands have transmission electrodes with high-frequency selectivity and good harmonic damping. A sub-strate (70mm*27mm) with a dielectric-continuous of 2.65 and a depth of 0.5mm was used for the design. the first pass band was centered at 2.5GHz while the second passband was centered at 5.3GHz with fractional bandwidths of 29.1% and 16.5%, respectively.

In 2012, A. Mason, A.Shaw, et al:

To examine the functioning of a new microwave sensor with an application in vital medical conditions. Where the sensor is placed in the pipeline used to pump the material of interest. This work takes into account the value of the sensor for monitoring whole blood in expansion into other large fluids such as cerebrospinal fluid. Thus the sensor has detected applications in other areas. Whereas, discovering that there is no connection at the moment for a few explanations can be useful to proceed with the preparation of returns or joint productivity. It turned out that the distant work turned out to be an admirable thirst. It has appeared in the recently universally visible object allowed.

In 2013 Liu et al:

The SIR short circuit gradient impedance resonator and this circuit were used to design a three-band dual –band compressed filter. The SIR hairpin shape, which can provide two resonant ways in two pass bands while maintaining great performance, served as the foundation for the downsizing process. the structure consisted two sets of resonators, first one was a dual-band SIR hairpin to generate the first and the second pass through bands while the second resonator was a short –circuited resonator loaded to generate the third pass pand. the base frequencies of the three traffic bands were discovered at 1.57GHz_GPS, 3.5GHz_WiMAX, and 5.2GHz_WLAN with partial bandwidth by 5.92%, 9.71%, and 5.5%, respectively. Using a sub-strate with dielectric continuous if thicknesses of 4.5 and 0.8mm, the design was simulated using anosoft HFSS. The finished circle was 15.2 mm by 12.6 mm.

In 2014 Shaman et al:

The filter consisted of a Line Coupled Modified Fork Resonator 3 polos. Suggested a compact microstrip bandpass mesh for mmW requests. The modifications were to perform a stepped impedance resonator (SIR) on the hairpin lines to suppress the avoided spurious harmonics, and to get broadcast zero proximate to the complex edge of the passband to improve the discrimination. The electrical length of the mesh was about a half-wave-length at the mid-band rate. The design was carried out using full-wave EM simulation on a TR/Duroid 6002 sub-strate with a depth of 0.129mm and a dielectric continuous of 2.94mm. Also, the filter has been made experimentally, and satisfactory agreement has been attained. The center frequency was 34GHz with a very wide stop-band with a refusal equal healthier than 10dB. The filter size was 2.45mm by 1.46mm.

In 2016, Carolin Reimann and Margarita et al:

Elucidated microstrip sensors for the biological tissue the agnostic therapy. The main components of this sensor needle-like operation appliance are oval SRRs that operate in a replication run between 8GHz and 12GHz. The resonator-based system has advantageous properties in recognizing little relative permittivity changes due to malignancies in biological tissue. When the sensor was piled with apparitions mirroring solid compared to tumorous tissue, a recurrence move of 350MHz was measured. thus warm removal therapy can be achieved by extending the input control at the specific reverberation repeat to 2.1W. A removal zone of 1.2cm×1cm×0.3cm was selected for warm affections with a test of ex-vivo meat liver.

In 2016 Shaman et al:

For motorized radar systems, a small wideband millimeter-wave-pass (UWB) filter has been developed. Two quarter-wavelength parallel segments are taken into account by the filter. Between the parallel-coupled lines, a shunt ring resistor and a shunt stepped-impedances open-circuited stub were placed to provide dispatch zeroes on each side of the pass band and increase selectivity. The RT/droid 6002 substrates with a dielectric constant of 2.94 and 0.127mm depth were used to implement the mesh approach. The mesh was realized by EM simulation and also was verified practically with decent contract amid fake and stately grades. The UWB spectrum obtained was ranging from (22-29GHz) centered at 25.5GHz with less than 3.7db insertion loss at the mid-band frequency and 22% fractional bandwidth.

In 2017 Xing et al:

A quintuple-mode resonator(QMR) was used to project a twin-band/pass filter with center-frequency independent comtrol and wide-band boosting. The candidate demonstrated that five conditions can be achieved by analyzing the data using odd and even methods. The first two methods were used for the deign of the inferior passband, though the other three methods were used to attain the higher pass/band. Compact size and tunable passband were obtained by manufacturing the filter on a rogers4003C substrate with a dielectric constant and thickness of 0.508mm of 3.55. Passband frequencies having a fractional bandwidth of At 2.96 and 5.695 GHz, respectively, 27.7% and 23.4% were concentrated.

In 2017, Sandra Costanzo:

The importance and physical criteria were talked about by choosing microwave and millimeter waves for the non-invasive monitoring of organic parameters. Currently, the current limitations within the microwave biosensor plan parameters have been set with modern views side by side to advance the accuracy of future executions. Particularly highlighted is the importance of accepting the variance of the unlucky deviation frequency of the organic radiation medium within the microwave sensor plan. Validation has been talked about within the glucose monitoring system. The concepts developed in the presentation work are intended to provide valuable starting bases within the use of solid, non-invasive monitoring frameworks based on microwaves or millimeter waves as excitation sources for biomedical applications.

In 2017, Nikolina Jankovic and Vasa Radonic:

A micro field sensor has been proposed. The sensor consisted of two resonances consisting of a collapsed microstrip line stacked with interdigital stubs. The resonant loads in two free-flowering modes. In this way, the simultaneous identification of two operators with a single reading system is authorized, to clarify the possibility of formation. Thus, a multilayer sensor was planned and fabricated with the proposed two-hole micro-field resonator. The one wound has a band between the lines between the toes and the other is located below the heel. The interaction of the sensor with different fluids was measured and a double guaranteed detection capacity was obtained, zero combined effect in addition to a measurement and effect comparable to other distributed microsensors. By making the structure's geometry more efficient, it can be put into practice even more. The suggested sensor has excellent potential for microfluidic applications like fluid mixing and cytometry as well as dual sensing applications.

In 2018 Zheng et al:

Introduced a unique idea for connecting microwave-band with millimeter-waveband in one filter. The submitted filter was used at dual/tri-band freqquencies. Based on stepped-impedance resonator principles and a low-pass mesh, a realistic microwave BPF with a large stop/band up to the mmW band was developed. The design technique is based on the aperture coupling mechanism. The filter consisted of three parts, the first part was a low-pass filter for getting the microwave-band frequency, and the second part was a stepped-impedance resonated based filter for ultra-wide stopband up to the millimeter-wave region, and substrate –integrated waveguide-based filter was used to obtain millimeter-wave frequency. The filter was created on three areas of RT/duroid5880 dielectric substrates of 2.2 dielectric constant and 0.508mm thickness and conducting materials. The simulation was performed using full-waveHFSS, and the filter was also fabricated practically with good contract amid pretend and extent fallouts. The cut-off frequencies obtained were centered at 2.4 and 30GHz. This dual-and filter was also modified for a tri-band operation by some adjustments to the design to give a third cutoff centered at 5.2GHz. the proposed filter can be used at aerials, power speakers, low-noise loudspeakers, and so along.

In 2018 Xiong et al:

A triple wideband filter (TWB-BPF) was introduced. It was distinguished by its small size and high isolation between traffic bands and multiple transmission zeros(TZs). Based on the principles of a multi-mode resonator(MMR) the design was created. Ten TZs were obtained to enhance the isolation from one band to another and to extend the suspension range by using odd and even mode analysis. TWB-BPFwas manufactured on rogers 4003substrate with a thickness of 0.508mm and 3.38 dielectric. The operating frequency was centered at 1.07, 3.25, and 8.32GHz with fractional bandwidth of 37.4%, 43.5%, and 40.4%, respectively. Decent contract was obtained between the simulation and the unhurried outcome. The previous survey focused on two parts, the first part was related to the design of dual/multi-band BPFs in mostly microwave bands using the gradient resistance resistor theory to get the beast out-of-band rejection and small size, while the second part was related to the design of millimeter-wave BPF. There is a lack of research looking at designing dual-band filters that can operate in the millimeter-wave and microwave bands simultaneously. This work will demonstrate the design of multiband BPF in the microwave band, and dual-band BPF in the millimeter wavelength and microwave bands.

In 2018, Taha A. Elwi:

The possibility of using palm filaments within the microwave industry was discovered for a new request related to the reproduced circuit receiver wires. The circuit is printed on the MTM structure based on a dipole antenna for Wi-Fi applications. This consideration has been given due to its possible position. By combining IPTR and NONP in PE casings at a ratio of 3.4/0.1/6.5, the sub/strate is prepared. For use in the numerical plan and examination, the customizable electromagnetic parameters are computed based on test estimations of the T-cap resonator in the relevant frequency region. At 3.106-j0.0314 and 1.548-j0.0907, respectively, we independently found r and r. The MTM architecture is printed using IJPT on an InP substrate based on SNPCI, but copper tape is added to both sides to generate the arils=dipoles. The S11 and energy designs of the receiving wire employment are mathematically examined utilizing CST MWS and HFSS re-pictures.

In 2018, Paris velen, katin gerenier2 et.al:

Based on the congruence of non-separate asymmetric lines, an unused type of microwave sensor has been proposed, such as one stacked with OCSRR, This is related to estimating the solute concentration in liquid arrangements and estimating the complex coherent segregation in liquids. For this reason, liquid channels are included in the best OCSRRs. The detection guide is based on miscalculation included in the cross-mode and is exceptionally sensitive to little irritation between the reference fluid, which is immersed in one channel, and the fluid below the test (LUT), which is pumped into the other channel. To determine the attentiveness of sodium in Di water the proposed sensor was used. It has been shown that the sensor exhibits amazing susceptibility to influence and can distinguish sodium concentrations less than 0.25g/L. For the classification of dielectric fluids, Although a mixture of DI water and ethanol was employed for standardizing resolutions, the benefit was confirmed by the consistently complex dielectric measurement of methanol arrangements in DI water. Moreover, the investigation of susceptibility to impact, based on the comparative circuit width of the planned instrument and large for Few inconveniences, was carried out. From this investigation, strange plan bases for sensing plans were collected.

In 2019, Taha A. Elwi and Omer Almukhrat Tawfeeq et. al:

They demonstrated in their inquiry for a Hilbert metamaterial printed radio wire based on natural biotope substrates, that green reuse potential is achieved by conducting natural plant residues used for green biosynthesis. For this, the printed and powered MTM radio wire is represented by the ETCPW support chassis as in the case. The strategy received for creating IPTR substrates to qualify pilot manufacturing conditions is investigated. Through this, the effect of handle fabrication on the εr and μr substrate is investigated. It was discovered that the thickness of the fabric had a surprising impact on the substrate's electromagnetic characteristics. In addition, binding and substrate roughness was found to expand rapidly with increasing tissue thickness. In this way, the MTM fix is printed onto the ordered IPTR substrate. Implementation of radio wiring constructed to provide UWB coordination impedance is measured at frequencies from 2.4 to 10 GHz.

In 2019, Ali M. Albishi and Seyed H. Mirijahanmardi et.al:

Provided by investigating microwave detection frameworks intelligently. The framework relies on balancing and reconfiguring the iteration interaction of various closely removed sensors over a wide iteration range. Below the postulation that bodily limits to be described such as liquid attentiveness are consistent over the sensor's repetition range, interactions that are characterized as vectors for several measurements of transmission coefficients are used at that point to develop and test 205 models built utilizing Neuroregulation strategies. Also, to expand scalability. Numerous tiny, indistinguishable electrical resonators are utilized for higher repetition rates. Three identical CSRRs were used in this study. The frame was used to try to gauge the liquid's concentration. A vector organization analyzer was used to record the data after PCB innovation was used to create the sensing portion of the frame. The outcomes were then utilized to create models for Bayesian-directional inverse propagation using an artificial neural network (BRANN). To describe fluids, models were utilized. BRANN can produce enough data even though the data sets were often small because of the utilization of several vector components as input. models with planes of truth between 83% and 99%. 90 percent of the data were used, resulting in a 94% accuracy level. The impact of resonator shape on field transmission surrounding the resonator and in tissues has not been fully explored in any of the aforementioned research, but it has been discussed in passing. Furthermore, past description techniques used in this kind of research still use relatively little of the invoked AI processes.

In 2020 Taha A. Elwi et.al:

Recent developments include the creation of a microwave sensor based on Moore fractal geometry for industrial applications. In that design, the authors applied their detection using a neural network for qualifying the quality of oil derives. The design was operating at 1.2GHz with a high insertion loss. The general size has not exceeded $40 \times 80mm^2$. The design was found to be a very reliable technique where most the nonlinear effects were eliminated accordingly.

In 2021 Taha A. Elwi et.al:

For biomedical applications, a different split ring resonator-based design was made available to measure the level of urea. The design was constructed from a transmission with open stub were connected to the split ring resonator to increase the system quality factor at 2.4GHz. The detection process is companied through matching the effects of the urine interdiction a plastic sink with low thickness. The detection process is optimized based on curve fitting and calibration equation process.

In 2022 Tanveerul Haq and Slawomir Koziel:

This paper proposes a new way for standardizing and redesigning complimentary split ring resonators quickly (CSRR). To enable quick tweaking of geometric parameters and optimization of CSRR over a broad range of operating frequencies, it also incorporates two inverse surrogate modeling approaches industrialised with the optimized resonator data. As the circuit superiority factor rises, tuning is controlled to accurately establish the operational frequency. For the analyzed circuit, its computing cost is as little as two EM analyses (not counting the inverse model setup). geared near use between 5 and 20 GHz. A course system analyzer was used to build and experimentally legalise the adjusted design for 15 GHz.

1.4 AIM OF THE THESIS

The major goal of the thesis is to build and test a microwave sensor for a non-invasive testing approach to detect blood glucose levels close to diabetics using a fractal microwave-resonator duplicated on a FR-4 substrate. The open stub inverted Meander line (OSM) architecture and an interdigital capacitor are the foundations of the fractal (IDC). A microstrip line is introduced to feed the proposed structures to meet the requirements of detection at certain frequency band with a small size and simplify the design process. This design relies on an LDR resistor for detection applications. The overall design size is fixed to 30mm×60mm.

1.5 THESIS OUTLINE

This research work of thesis breack down to 5 chapters presented as trails:

Chapter_1: Shows a basis of work, and a literature survey shows the prior studies in this field.

Chapter_2: Contains visionary background about microstrip resonator and their design, stepped-impedance resonators theory, parameters descriptions of the used materials, and applications for microwave resonators.

Chapter_3: Contains the design and simulation of the proposed resonator based on compact stepped-impedance meander line operating in the microwave-band range.

Chapter_4: It offers and discusses the obtained results based on simulation and measurements of the proposed sensor.

Chapter_5: Explains the decisions and proposals for future effort.

2.THEORETICAL BACKGROUND

2.1 OUTLINE

In this episode, an impression of microwave resonators and their requests in wireless message is presented. Also, the specifications of the microstrip structure and materials were presented. In addition, the specifications and analyzes of the gradient resistance resonators were presented.

2.2 OVERVIEW OF RF MICROWAVE RESONATORS

The frequency range of microwave and radio waves (RF)covers signals with a frequency span(100GHz-1000GHz). It is referred to VHF whose extended frequencies are (30-300MHz), while the frequency(300-3000MHz)is called UHF. The period microwave is charity for frequency between 3GHand300GHz with an electric wavelength between 10cm and 1mm apart. Millimeter waves are signals of wavelength within the order of millimeters. Building on R/F and microwave has a variety of applications. As illustrations, they can be used in radar framing, framing, recalcitrant restorative, detection, etc.

In RF/Microwave applications, the microwave resonator is crucial. The primary function of microwave resonators is to reject the unwanted signal spectrum and allow the specified signal spectrum to pass. Applications are amplified from excitation frameworks such as fawning Tv, and therapeutic, to military radars. In the remote communication framework, microwave and RF resonators are widely used, and the cellular communication framework provides strict channel requirements in base stations and multi-use stations such as telephones. In figure 2.1 a square diagram is shown from the RF front end of the base station. One of the diagram's most significant dynamic transmission line kinds, and one that microstrip lines frequently use , focal points are created on the white optical shapes, and this includes the reasonableness of their miniaturization is simpler and can be combined with all of the microwave tools inactive and dynamic figure 2.1 the external shape of the microstrip is illustrated in the conduction sector(microstrip line), with thickness T and width W, with thickness H (the relative dielectric constant r) at the top and ground level at the bottom of the insulating substrate (conductor).

For BAN applications, IEEE 802.15.6-compliant antennas operate in the 3.75–4.25 GHz Low UWB range. The back and abdomen were meticulously measured and imitated to produce the characteristics of the body. The antenna has proven to be a useful part of body area networks. This research looks at antenna matching close to the human body. The grounded structure is further compared using frequency and time domain data. Using models and experiments, antenna propagation efficiency is calculated in free-space. On-body investigations were used to put an end to these inquiries. A variety of antenna layouts were used to assess the placement of antennas on the bellies and backs of human participants, particularly at the navel level Computer models came first, then measurements and observations were made in the real world. The performance of the antenna was in great accord with simulation and measurement results. The BAN applications benefit from all we've learnt about antenna operating from this work.

This work illustrates wearable textile antennas with dual bands and dual sensors. While WBAN and WLAN applications operate at a frequency of 2.450GHz, GPS operates at 1.50GHz. To reduce backward contamination and increase aerial gain, a 2.405GHz band-based AMC plane-based antenna has been developed. Cells for square patch units measure three by six and have four built-in slits and a square ring. When the stove is placed on top of the substrate, it resembles a square patch. The four corners of the heater each have a rectangular slit that permits the dual-band utilization of the circular polarization property of the GPS band. On the 2.405GHz band and the 1.575GHz band, respectively, the antenna generated realized gains of 1.904dBi and 1.908dBic. An indoor and outdoor accurate position tracking system using a textile antenna with dual groups and dual IDs was developed. The dual band radiator's initial shape, intended to function at both 1.505GHz and 2.405GHz, was a rectangular patch with smaller angles (with linear division). AMC was created primarily to make wearable probes smaller in shape. Under the feeler is a collection of element cells. The 2.434GHz AMC unit cells are constructed up of square patches with fair bands and rectangular slots on either side. The 1.5733GHz band provides an axial ratio bandwidth of 9% at 3 dB for these two bands, with total fractional impedance bandwidths of 27,4% and 7,55 percent. At 1.585GHz, one may anticipate seeing 1.92dBic, but at 2.495GHz, it has 1.984dBic. When the antenna was studied while being bent, it was discovered that it functioned best when bent along the body's y-axis. Only AMC aircraft antennas with SAR values less than 0.12W/kg are permitted to be worn on the upper arm or shoulder. As its front to back ratio, which frequently exceeds 10 dB, is under the 2W/kg constraint, it is suitable for wearable applications. Particularly in high data rate multiple input multiple output (MIMO) and orthogonal frequency division multiplexed (OFDM) systems, spectrum precoding has a significant impact on system performance overall. Two mask-compliant spectral precoding techniques show how the inherent degrees of freedom of (large) MIMO systems can be used to lower TxEVM at the receiver and increase system throughput. Furthermore, we offer the TOPADMM algorithm, a three-operator consensus alternating direction method of multipliers (ADMM), which divides a challenging problem into manageable chunks that can be resolved more quickly. Using a TOP-ADMM-based strategy, the issue of spectral precoding is resolved. An important set of numerical discoveries are used in our third contribution, which makes use of a simulator that complies with NR version 15. Out-of-band emission (OOBE) criteria can be met even if the transmitter possesses perfect channel information if the suggested substitutes deliver the same block error rate and throughput performance. Yet, even when throughput gradually decreases with channel uncertainty, OOBE efficiency is unaffected. There are considerable issues with dynamic beamforming algorithms in tall-rapidity bar nets because of the predicted high speed trains (up to 500 km/h). Considering that HSR cellular networks are linear, it is possible to anticipate the path of the train practically perfectly. Fixed beamforming, which uses highly directional antennas with predetermined emission directions, is a less expensive option to dynamic beamforming. To facilitate the use of fixed BF in HSR mmWave communications, the performance gap between lively BF and secure BF must be investigated. In order to conduct empirical analysis, this study uses raw data that were obtained through extensive measurement operations. The high-speed rail tunnel and regular railroad station are two locations where trains can be observed most frequently. [21]-[25].

It offers an examination of the received signal's intensity, power deflection pattern, and root-mean squared delay. With the information obtained, we broaden the often used close-in freespace (CI). To improve the overall model's ability to accurately describe the PL there, model the PL in the HSR tunnel. Thus, using the enlarged model and the observed data, one may contrast dynamic BF with constant BF. We discovered that the throughput in the train station was 21% higher than the throughput in the dynamic BF even with significant beam misalignment. High data speeds are made possible by energy efficiency, which is essential for wireless communications. D2D is a viable technique for creating energy-efficient gadgets and cellular networks with plenty of antennae. Cellular users interfere with D2D pairings, but D2D couples interfere with one another. The BS also has an impact on D2D couples. To manage multi-D2D communications via multiple antennas, the BS has developed resource allocation algorithms that are both energy-efficient and multi-D2D compatible. The Dinkelbach algorithm, the Message Passing Algorithm (MPA), and multi-layer artificial neural networks are used in our strategy to boost global energy efficiency while satisfying the data rate needs of both cellular users and D2D couples. [25]-[27].

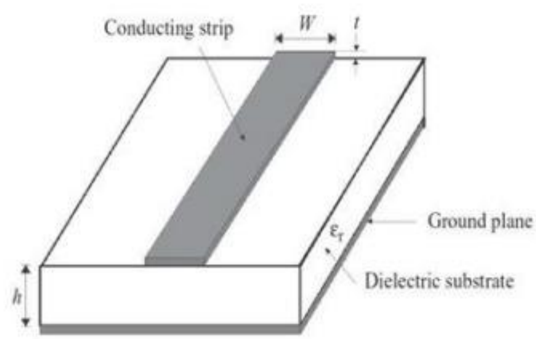

Figure 2.1: General microstrip structure.

Figure 2.2 shows the outline of the field lines development. A fact is that the dielectric does not fill the area above the tape, resulting in a more complex microstrip examination and behavior. The microstrip has a heterogeneous structure, where the field propagates from two media and discusses the beating and the insulator from the foot, which makes the microstrip not support the unadulterated TEM wave. This could be an internal reason for the pure TEM wave because it was a transverse component and propagation velocity was based as it was on the fabric characteristic. The penetrability(μ), permittivity(ε). The waves in a microstrip line, however, will not have vanishing longitudinal components of electric and attractive regions and their propagation speed will not depend, as it did previously, on the property of the fabric, but rather on that of the microstrip texture when navigable wave media (insulating substrate and discussion) are present. The longitudinal components of the region are excluded when they are smaller than the transverse components within the crushing mode of the small bar. In such a case, the crushing mode at that point works like the TEM method. And the idea of a TEM transmission line is serviceable in a microstrip streak as fine. It is usually called a quasi-TEM guess and is substantial during greatest of the work microstrip repeat varieties.

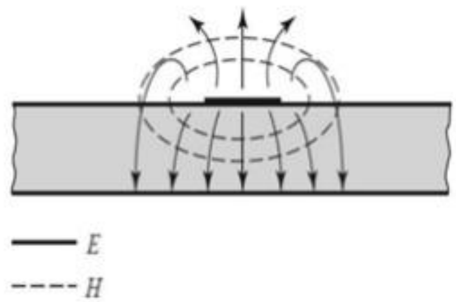

Figure 2.2: fields distributions.

Microwave resonators may take on distinctive characteristics based on the cut-off frequency of the selected mark. Low-pass, high-pass, band-pass, and bans switched microwave resonators are among the most common types of microwave resonators. In figure 2.3 the weak properties of microwave resonators are shown.

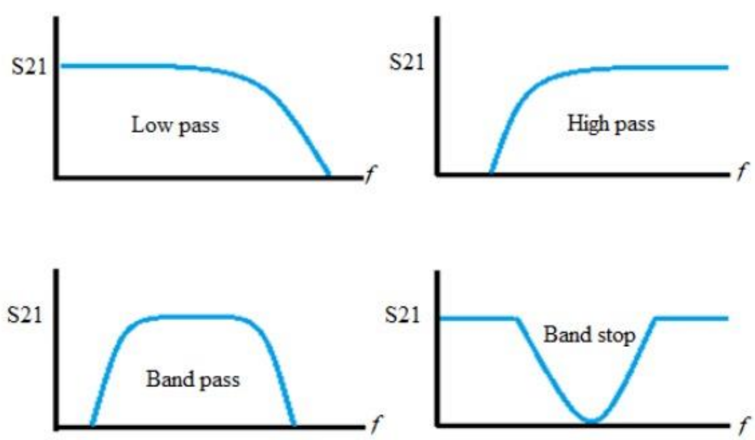

Figure 2.3: filter attenuation characteristic

2.3 MICROSTRIP FILTER

Microstrip development consists of three parts. Are conductive of fabric width W and thickness t on the best insulating subs/trate with a constant comparative dielectricε-r and depth h. both of the previously mentioned parts were placed on a conductive ground level. The geometric arrangement is defined in fig(2.1). the microstrip structure is heterogeneous so it does not support pure TEM waves since the region are generated by two media (discussed at best and dielectric at the foot), and their resulting delay depends on permittivity ε and transmittance μ.

2.3.1 Effective Dielectric Constant, Characteristic Impedance, and Attenuation

For microstrip outlines, the real dielectric endless approximates the following equation expression

$$\varepsilon_e = \frac{\varepsilon_r+1}{2} + \frac{\varepsilon r-1}{2}\frac{1}{\sqrt{1+\frac{12d}{w}}} \tag{2.1}$$

The phase velocity (υρ) and the propagation constant (β) are given by:

$$\upsilon\rho = \frac{c}{\sqrt{\varepsilon e}} \tag{2.2}$$

where c is the speed of light which is approximately ($3 \times 10^8 \mathrm{m/s}$).

$$\beta = \frac{2\pi}{\lambda_g} \tag{2.3}$$

λ_g is the guided wavelength and it is expressed as :

$$\lambda_g = \frac{300}{f(GHz)\sqrt{\varepsilon e}} \quad (mm) \tag{2.4}$$

The characteristic impedance(Zo) of a microstrip line I given by:

$$Zo = \left\{\frac{60}{\sqrt{\varepsilon e}} ln\left(\frac{8h}{w} + \frac{w}{4h}\right) \qquad \text{for } \frac{w}{h} \leq 1\right.$$

$$Zo = \frac{120\pi}{\sqrt{\varepsilon e}\,(W/h+1.393+0.667ln(w/h+1.444))} \qquad \text{for} \frac{w}{h} \geq 1 \tag{2.5}$$

For a giving characteristic impedance (Zo), the $\frac{w}{h}$ the ratio can be found by :

$$\frac{w}{h} = \left\{\frac{8e^A}{e^{2A}-2}\right. \qquad \text{for } \frac{w}{h} < 2$$

$$\frac{w}{h} = \frac{2}{\pi}\left[B - 1 - ln(2B-1) + \frac{\varepsilon_r - 1}{2\varepsilon_r}\left\{ln(B-1) + 0.39 - \frac{0.61}{\varepsilon_r}\right\}\right] \text{for} \frac{w}{h} > 2 \tag{2.6}$$

Where A= $\frac{Zo}{60}\sqrt{\frac{\varepsilon_r+1}{2}}+\frac{\varepsilon_r-1}{\varepsilon_r+1}\left(0.23+\frac{0.11}{\varepsilon_r}\right)$, and B= $\frac{377\pi}{2Zo\sqrt{\varepsilon_r}}$

The attenuation due to dielectric losses for a microstrip line can be expressed by:

$$\alpha d \approx \frac{ko\varepsilon_r(\varepsilon e-1)\tan\delta}{\sqrt[2]{\varepsilon e}\ (\varepsilon_r-1)} \quad \text{(Np/m)} \tag{2.7}$$

Where $\tan\delta$ is the loss tangent of the dielectric, and ko = $\frac{w}{v}$ the attenuation due to the conductor losses is expressed by:

$$\alpha d \approx \frac{Rs}{ZoW} \tag{2.8}$$

Where Rs =$\sqrt{w\mu o/2\sigma}$ es la resistividad superficial del conductor. En la mayoría de los sustratos, la pérdida del conductor es más importante que la pérdida dieléctrica.

2.4 DISCONTINUITIES IN MICROSTRIP ELEMENTS

Figure(2.4) shows the structure of some outages and their similar circuits. The most common outages are in the microstrip, also called stubs it is open ends, variable measurement steps, cracks between conductors, torsions, and junctions.

2.4.1 Open-End Circuit

The microstrip line is open-ended as shown in figure (2.4). an equivalent capacitance must be connected so that a goldfield occurs at the physical end of the conduction strip. This regulating field can be modeled with the shunt capacitance or the length of the transmission line. The relationship can be expressed by:

$$\Delta l = \frac{\mathrm{C}ZcCp}{\sqrt{\varepsilon_r e}} \tag{2.9}$$

2.4.2 Steps

Figure 2.4(b) shows the step structure and its equivalent LC circuit. The formulas for capacitance and inductance are approximated by the equations below:

$$C = 0.00137h\frac{\sqrt{\varepsilon_r e1}}{Zc1}\left(1-\frac{W2}{W1}\right)\left(\frac{\varepsilon_r e1+0.3}{\varepsilon_r e1-0.258}\right)\left(\frac{\frac{W1}{h}+0.264}{\frac{W1}{h}+0.8}\right) \quad \text{(Pf)} \tag{2.10a}$$

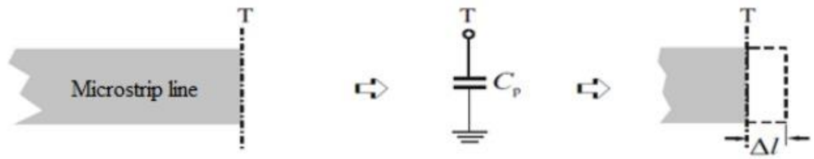

(a)

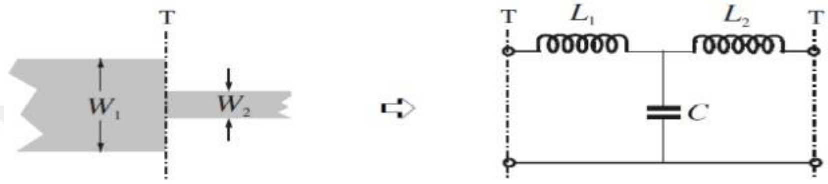

(b)

(c)

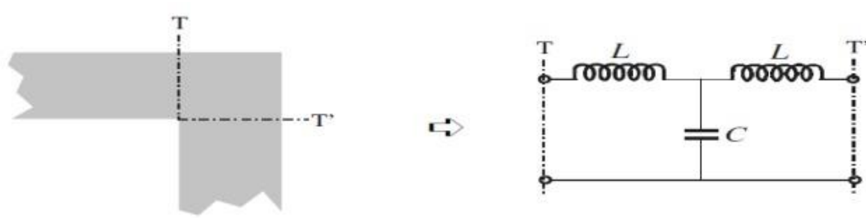

(d)

Figure 2.4: microstrip discontinuities:(a)open-end; (b)step; (c)gap; (d)bend(figures.

$$L_1 = \frac{L_{w_1}}{L_{w1}+L_{w2}} L, \quad L_2 = \frac{L_{w2}}{L_{w1}+L_{w2}} L \qquad (2.10b)$$

$$\text{With } L_{wi} = Z_{ci}\frac{\sqrt{\varepsilon_r ei}}{c}, \; L = 0.000987h\left(1 - \frac{Zc1}{Zc2}\sqrt{\frac{\varepsilon_r e1}{\varepsilon_r e2}}\right)^2 \qquad \text{(Nh)}$$

Where W1 and W2 are microstrip width, while Zci and $\varepsilon_r ei$ are the characteristic impedance and effective constant related to the width Wi.

2.4.3 Gaps

In figure 2.4(c), the shunt capacitors and series circuits equivalent to the microstrip gap are shown. The capacitances can be determined by:

$$C^{p} = 0.5C_{e} \qquad (2.11a)$$

$$Cg = 0.5Co - 0.25C_{e} \qquad (2.11b)$$

Where

$$\frac{Co}{W} = \left(\frac{\varepsilon_r}{9.6}\right)^{0.8}\left(\frac{s}{W}\right)^{mo} exp(Ko)(\text{Pf/m})$$

$$\frac{Ce}{W} 12\left(\frac{\varepsilon_r}{9.6}\right)^{0.9}\left(\frac{s}{W}\right)^{me} \exp(Ke)\ (\text{Pf/m})$$

And

$$\text{Mo} = \frac{W}{h}\left[0.619\ log\left(\frac{W}{h}\right) - 0.3853\right] \text{ for } 0.1 \leq s/W \leq 1$$

$$\text{Ko} = 4.26 - 1.453 \log\left(\frac{W}{h}\right) \qquad m_{e} = 0.8675 \text{ for } 0.1 \leq s/W \leq 0.3$$

$$K_{e} = 2.043\left(\frac{W}{h}\right)^{0.12}$$

$$m_{e} = \frac{1.565}{\left(\frac{W}{h}\right)^{0.16}} - 1 \qquad \text{for } 0.3 \leq s/W \leq 1$$

$$K_{e} = 1.97 - \frac{0.03}{W/h}$$

2.4.4 Right Angle Bends

In figure 2.4(d), the small strip is shown bent at right angles to its parabolic grid. The derivative formulas to represent capacitance and inductance are expressed as follows:

$$\frac{C}{W}\left(\frac{pF}{m}\right) = \begin{cases} \dfrac{\frac{(14\varepsilon_r+12.5)W}{h} - (1.83\varepsilon_r - 2.25)}{\sqrt{\frac{W}{h}}} + \dfrac{0.02\varepsilon_r}{\frac{W}{h}} & \text{for} \frac{W}{h} < 1 \\ \dfrac{(9.5\varepsilon_r+1.25)W}{h} + 5.2\varepsilon_r + 7 & \text{for} \frac{W}{h} \geq 1 \end{cases} \qquad (2.12a)$$

$$\frac{L}{\text{h}} = 100\left(\sqrt[4]{\frac{W}{h}} - 4.21\right) \qquad (2.12b)$$

2.5 MICROSTRIP RESONATORS

Here, different types of microstrip resonators are shown and examined. The dual impedance_ vibrato, toroidal_ vibrato, twisted-loop vibrato and integrated substrate vibrato are the most commonly used resonators.

2.5.1 Stepped-Impedance Resonator(SIR)

In figure 2.5, the SIR structure is shown, which is a non-even program line consisting of two regions big-resistance and smal-impedance sectors.

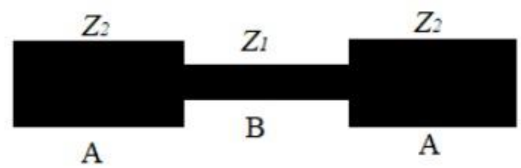

Figure 2.5: Diagram of the Treaded-impedance vibrato.

The typical impedance of each line region is denoted as z-1 and z-2 with separate electrical spans A and B. The say inductance can be connected by:

$$\text{Yin} = \frac{2jY2(KK1+K2)(K-K1K2)}{K(1-K2^2)(1-K2^2)-2(1-K^2)K1K2} \quad (2.13)$$

Where K1=tan $\left(\frac{A}{2}\right)$, K2=tan(B) and K=$\frac{Z2}{Z1}$. The SIR is used for assemblies that necessitate wide refusal ranges.

2.5.2 Square-Loop Ring Resonator

The structure of the square ring resonators is shown in figure 2.6. It consists of 4 indeterminate sides connected to the formation of a closed square circuit and coupling holes. If one of the join gaps is removed, the consequence of the toroidal resonators on the resonant frequency will be fewer and the modulation chaos will be reduced. Other ways to embed the coupling and reduce viewing difficulty are to protect the ring resonator with electrical insulation or to use copper tape tide over the notch.

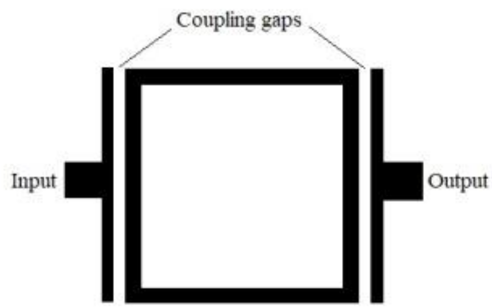

Figure 2.6: Estructura general del resonador de anillo de bucle cuadrado.

2.5.3 Meandered Resonator

In figure 2.7, a2D wind resonator with the same length and measurements as a 2D Hilbert resonator is shown. Meaning that the capacitance is equal with each set. Therefore, if the inductors do not rise to this point, then this means that Las frecuencias de resonancia serán diversas para cada estructura.

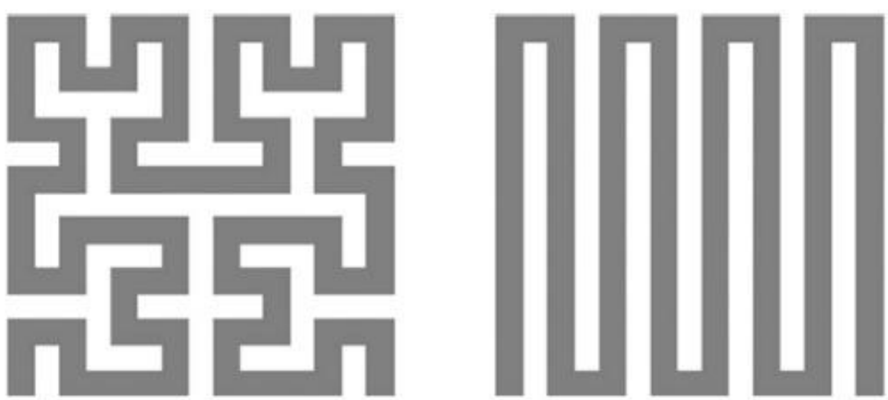

Figure 2.7: 2D zigzag and 2-D Hilbert printed circuit vibrato with the similar distance and space.

The meander's overall inductance per length , Ltot is given by:

$$Ltot = 2nl \quad (2.14)$$

Where L denotes the inductance pr distance for each straight streak portion and n denotes the number of meander attempts.

2.5.4 Substrate-Integrated Waveguide SIW resonator

Due to its low-cost contact point, compact metering, and unfortunate excellent integration with other waveguides and circuits, the demand for this resonator has steadily increased over time. A four-sided wave-guide with metallic slit mid-air slots connecting from the top layer to the ground layer of the waveguide is depicted as the SIW region in Figure 2.8. As a result, Da is the distance between the discussion gaps and the partition between them, while Sv is the panel between two together minerals finished without Dv being the coldness through each over.

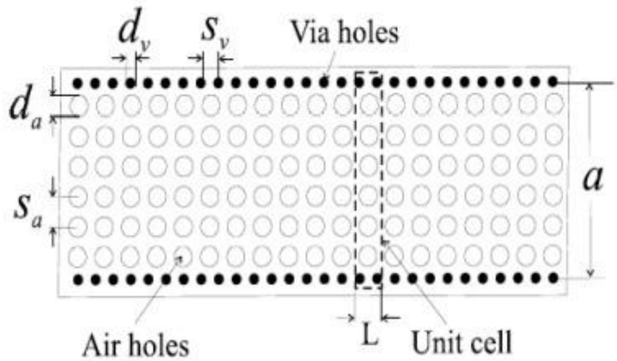

Figure 2.8: SIW resonator layout.

The SIW can be careful to calculate its true width using a four-sided wave-guide:

$$\alpha eff = \alpha - \frac{dy^2}{0.95Sv} \quad (2.15)$$

Metal slots are designed to transmit additional signs from the contribution to the yield docks, plummeting radiation loss with allowing for a small footprint.

2.6 COUPLING TYPES FOR TRANSMISSION LINES

Microwave resonators can be coupled in different ways. And each method produces a different resonance. Figure 2.9 displays the 3 kinds of link, namely: electric link, magnetic join, and varied-join.

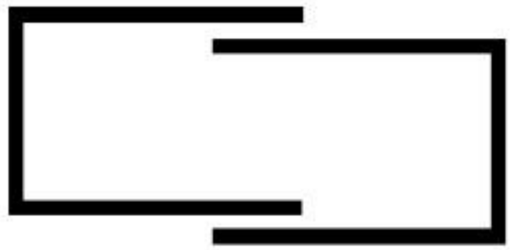

(a)

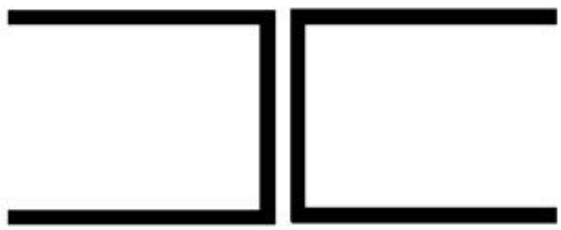

(b)

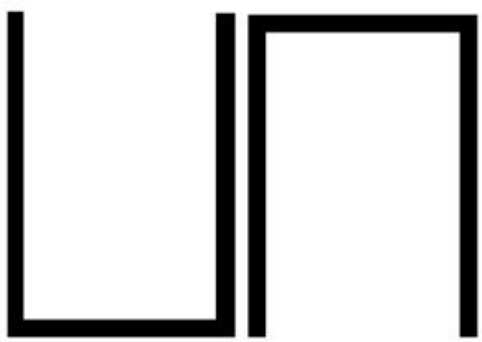

(c)

Figure 2.9: Broadcast Stroke Join Drawings: (a) Electrical; (b) magnetism; c) varied .

2.6.1 Electric Coupling

Figure 2.10(a) shows the assembled elements of the electrical coupling structure in figure 2.9(a). where L and C are characteristic conductive inductors and capacitors, to achieve from $1/\sqrt{LC}$ the booming incidence, and denote joint capacitor. The equal tour of figure

2.10(a) can be staggered with the circuit signified in figure2.10(b).

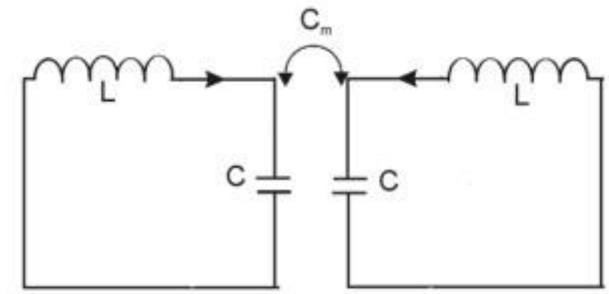

(a)

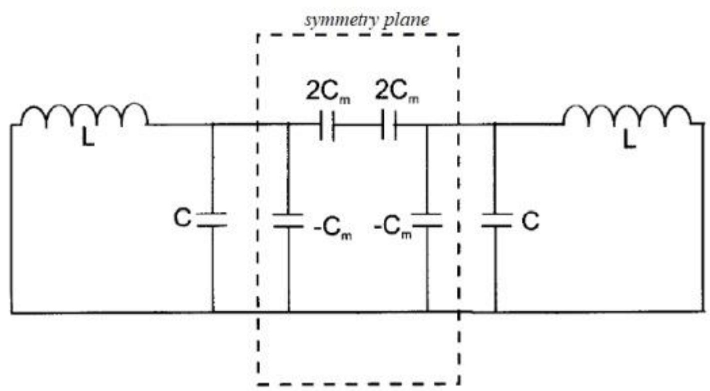

(b)

Figure 2.10: Electric link: (a) took equal component; (b) other from of an equal tour.

In figure 2.10(b) a tiny electrical tour (electric wall) in place of the symmetry planar, the resonant rate is given by;

$$f_e = \frac{1}{2\pi\sqrt{l(C+Cm)}} \tag{2.16}$$

this resonance frequency is inferior than that of the discrete actuator due to the link effect which raises the charge capacitance capacity of the signal resonator when the electrical barrier is embedded in the symmetric plan of joined actuator. Nowadays, substituting the level of symmetry in figure 2.10(b) with an exposed circuit (attractive divider), the tour resonance will be;

$$fm = \frac{1}{2\pi\sqrt{L(C-Cm)}} \tag{2.17}$$

if the recoil frequency is expended, the coupling effect reduces the ability to store a charge. Calculations (2.16) and (2.17) can be used to extract the electrical join number K-E

$$KE = \frac{f^2m - f^2e}{f^2m + f^2e} = \frac{Cm}{C} \quad (2.18)$$

2.6.2 Magnetic Coupling

Transmission Line Coupling Diagrams: (a) Electrical; (b) magnetism; c) Mixed The complex component of the attractive coupled resonator is shown from Fig. 2.9 (b) in Fig. 2.11 (a), where Lm denotes the complex inductor. The impedance reflector speaks of the attractive coupling between the two storm circuits. Figure2.11(a) can be rotated into a similar circle shown in figure 2.11(b). if the symmetry plane in figure2.11(b) a tiny circuit (electric splitter) is used in its place, the echo incidence can be assumed to be;

$$fe = \frac{1}{2\pi\sqrt{(L-Lm)c}} \quad (2.19)$$

When the electrical barrier is impedance within the symmetric plane, the resonant frequency expands due to the coupling effect which reduces the outward fluidity inside the signal actuator tour.

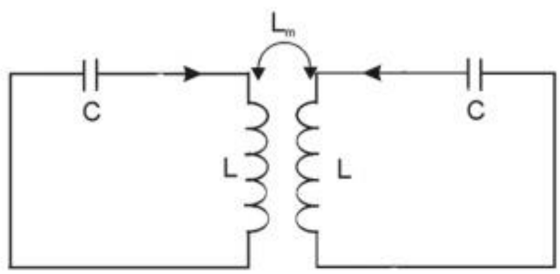

(a)

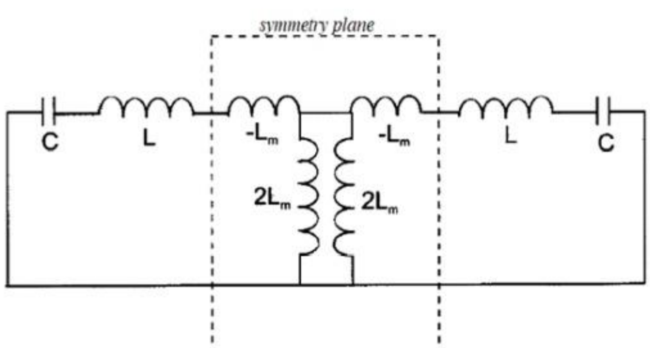

(b)

Figure 2.11: Magnetic connexion: (a) endured alike; (b) unusual from an alike circuit.

When it comes to motifs, an attractive divider (open circuit) rather than the symmetrical plana determines the bounce frequency;

$$fm = \frac{1}{2\pi\sqrt{(L+Lm)c}} \tag{2.20}$$

The resonance is diminished by the coupling effect which increases the removal flux. From the conditions (2.19) and (2.20), the good-looking connection number k-m can be create;

$$km = \frac{f^2e - f^2m}{f^2e + f^2m} = \frac{Lm}{L} \tag{2.21}$$

2.6.3 Mixed Coupling

Fig. 2.12 shows the assembled element of the paired composite assembly of Fig. 2.9(c). Also, by introducing an electric barrier and magnetic partition unique by one instead of the plane of symmetry in Fig. 2.12, resonance can be obtained as shown;

$$fe = \frac{1}{2\pi\sqrt{(L-L'm')(C-C'm)}} \tag{2.22}$$

$$fm = \frac{1}{2\pi\sqrt{(L+L'm)(C+C'm)}} \tag{2.23}$$

Both electric/magnetic influences must the similar effect on booming occurrence instable, as can be shown.

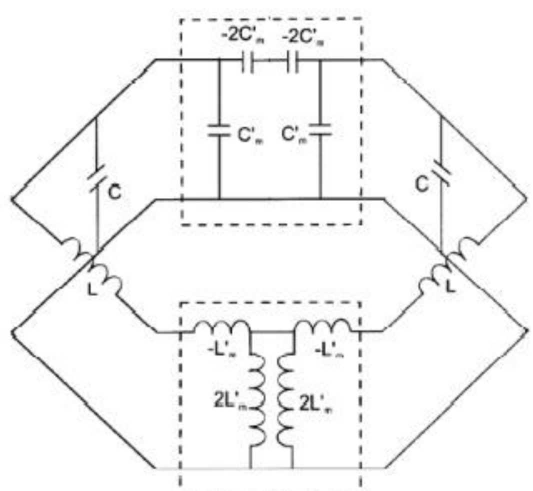

Figure 2.12: Mixed connexion limped portion.

By solving equations (2.22) and (2.23), the mixed coupling coefficient Kx is :

$$Kx = \frac{CL'm + LC'm}{LC + L'mC'm} = \frac{f^2e - f^2m}{f^2e + f^2m} \qquad (2.24)$$

2.7 COUPLING MICROSTRIP LINES

Dual lines are used for no reason within the microwave plan channel areas. Figure 2.13 shows the intersection area of the paired microstrip line. It consists of two parallel lines of width W and section S. These double linear coincidences can support two specific modes of TEM, single and real.

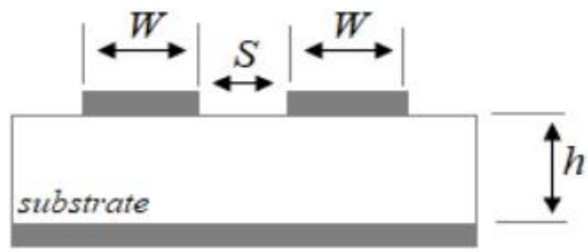

Figure 2.13: Cross-slice of coupled microstrip ranks.

2.7.1 Even Odd Mode Capacitance

When both microstrip lines have the same voltages (same sign charges), as seen in figure 2.14(a), the magnetic wall is formed, which is known as indeed mode capacitance. When both lines are connected and have separate possibilities (distinctive signal), this leads to the creation of an electrical divider and is called signal mode capacitance as shown in figure2.14(b). these two modes are simultaneously excited and undergo distinct permittivity which means that they are not non-adulterated TEM modes, so they reproduce at varied velocities. Odd and even capacitances are denoted as C_e and Co respectively and can be expressed as;

$$Ce = Cp + Cf + C'f \qquad (2.25)$$

$$Co = Cp + Cf + Cgd + Cga \qquad (2.26)$$

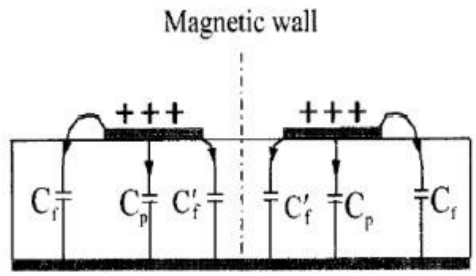

(a)

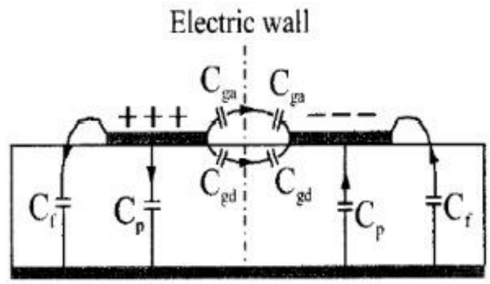

(b)

Figure 2.14: TEM modes for a couple of attached appearances; (a) smooth style; (b) strange style.

Where Cp and Cf are the parallel capacitors between the strip line and the pulverized and the fringe capacitance singly, which both are given by:

$$Cp = \varepsilon o \varepsilon_r W/h \tag{2.27}$$

$$Cf = \frac{\frac{\sqrt{\varepsilon_r e}}{CZc} - Cp}{2} \tag{2.28}$$

The parameter $C^{'}f$ denotes the adjustment of the fringe capacitance of a signal line due to the presence of the second line, it is expressed by:

$$C^{'}f = \frac{Cf}{1 + A\left(\frac{h}{s}\right)\tan\left(\frac{8s}{h}\right)} \tag{2.29}$$

Where $A = exp\left[-0.1exp\left(2.33 - \frac{2.53W}{h}\right)\right]$

$$Cgd = \frac{\varepsilon o \varepsilon_r}{\pi} ln\left[\coth\left(\frac{\pi s}{4h}\right)\right] + 0.65Cf\left(\frac{0.02\sqrt{\varepsilon_r}}{\frac{s}{h}} + 1 - \frac{1}{\varepsilon_r^{2}}\right) \tag{2.30}$$

$$Cga = \varepsilon o \frac{k(k^{'})}{k(k)} \tag{2.31}$$

$$\text{Where } k = \frac{\frac{s}{h}}{\frac{s}{h}+2\frac{W}{h}} \text{ and } k^{'} = \sqrt{1-k^2}$$

$\frac{k(k^{'})}{k(k)}$ is the ratio of the elliptic function and given by;

$$\frac{k(k^{'})}{k(k)} = \begin{cases} \frac{1}{\pi} ln\left(2\frac{1+\sqrt{k^{'}}}{1-\sqrt{k^{'}}}\right) & \text{for} 0 \leq k^2 \leq 0.5 \\ \frac{\pi}{ln\left(2\frac{1+\sqrt{k}}{1-\sqrt{k}}\right)} & \text{for } 0.5 \leq k^2 \leq 1 \end{cases}$$

2.7.2 Even Odd Styles

The impedances of the even-odd modes are indicated as Zce and Zco can be represented by;

$$Zce = \left(c\sqrt{C_e^a C_e}\right)^{-1} \tag{2.32}$$

$$Zco = \left(c\sqrt{C_o^a C_O}\right)^{-1} \tag{2.33}$$

Where $C_e^a$and $C_o^a$are capacitor for the tied line with air as a dielectric for the even and odd modes. The effective dielectric constant for even and odd modes are denoted as $\varepsilon_{re}^e$and ε_{re}^o respectively, and can be expressed by;

$$\varepsilon_{re}^e = \frac{Ce}{C_e^a} \tag{2.34}$$

$$\varepsilon_{re}^o = \frac{Co}{C_o^a} \tag{2.35}$$

2.8 MICROWAVE FILTER NETWORK VARIABLES AND PARAMETERS

RF and microwave resonators can be spoken of as two-port regulators as shown in figure2.15, where V1and I1 are the voltage and current factors in port 1 separately, and V2 and I2 are the potential and smoothing carrier factors in port2 individually. The terminal impedance is denoted as Zo1, Zo2, and Es speak to the source supply voltage. Current and voltage estimates at microwave frequency are a troublesome approach, so the factors a1,b1,a2, and b2 are given, as a and b are the sign of occurrence and reflected waves separately. The connections between voltage and current are given with wave factor as;

$$Vn = \sqrt{Zon}\ (a_n + b_n) \text{ n=1,2} \tag{2.36}$$

$$In = \frac{1}{\sqrt{Zon}}(a_n - b_n)$$

The power at point n is

$$Pn = \frac{1}{2} Re(V_n I_n^*) = \frac{1}{2}(a_n a_n^* - b_n b_n^*) \tag{2.37}$$

Where the * sign is denoted for the conjugate. It can be seen that the terms $a_n a_n^*/2$ and $b_n b_n^*/2$ are the incident and reflected wave power at port n respectively.

2.8.1 Scattering Parameter

The wave variables of a two-port networks scattering parameter (s-parameter)as;

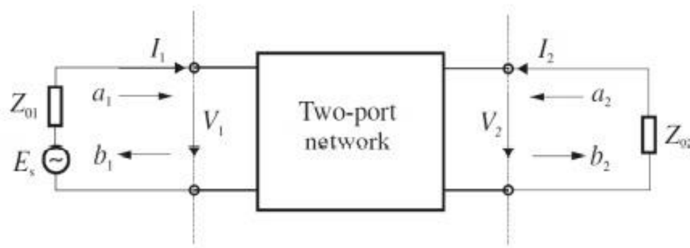

Figure (2.15): Two-port network

$$S11 = \frac{b1}{a1}\Big| \quad a2 = 0 \qquad\qquad S12 = \frac{b1}{a2}\Big| \quad a1 \tag{2.38}$$

$$S21 = \frac{b2}{a1}\Big| \quad a2 = 0 \qquad\qquad S22 = \frac{b2}{a2}\Big| \quad a1$$

The scattering matrix can be formulated as;

$$[S] = \begin{bmatrix} S11 & S12 \\ S21 & S22 \end{bmatrix} \tag{2.39}$$

The parameter S11 and S22 are the echo constants, where S12 and S21 are the broadcast constants. From the diffusing framework, two critical parameters are displayed; the inclusion misfortune IL and return misfortune RL. These two parameters can be communicated as;

$$IL(dB) = -20log|Smn| \qquad \text{m,n= 1,2(m} \neq n) \tag{2.40}$$

$$RL(dB) = 20log|Snn| \qquad \text{m,n=1,2}$$

As an alternative for the term (return loss), the voltage standing wave ratio VSWR can be used as;

$$VSWR = \frac{1+|S_{nn}|}{1-|S_{nn}|} \tag{2.41}$$

2.8.2 Filter Bandwidth and Fractional Bandwidth

The transfer speed is calculated at a 3dB point of the passband, which is the contrast between the high-band FH and the lower-band FL frequencies, is the channel transmission capacity BW;

$$BW = f_{3dBH} - f_{3dBL} \quad (2.42)$$

The fractional bandwidth FBW is the percentage of bandwidth divided by the center frequency fo of the passband;

$$FBW\% = \frac{f_{3dBH} - f_{3dBL}}{fo} x100 \quad (2.43)$$

The MPA factor graph for D2D pairings takes into consideration both interference at the base station (BS) and interference between D2D pairs. This is accomplished by training a deep neural network using a hybrid approach. It has been demonstrated that multi-D2D communications algorithms for efficient resource allocation outperform single-D2D communication methods. Our study focused on a wide range of problems, including wireless interchip communication between close ICs. To avoid destructive interference, it is advised to use symmetrical layers to guide the generated energy away from the receiving antenna and into the vacuum of space. EBG structures and soft/hard surfaces are the subject of extensive research in order to focus the emitted energy onto the receiving antenna. By reducing the spherical spreading losses caused by spherical radiation, the receiving antenna receives more power. This work presents a frequency diversity array (FDA)-based quadrature spatial modulation-based mm-wave communication system architecture (QSM). Spatial modulation techniques use the highest levels of modulation possible to achieve the desired results [20]–[25]. The computational complexity of an ML-based sensor skyrockets at the receiver. Phased array (PA) SMT systems are also employed, however they only provide oblique communication. For range-angle dependent QSM wireless communications, we advise using a conventional FDA based on a moderately linearly rising frequency set across the array. Data is transmitted by vectors with a small amount of frequency variation. We recommend a suboptimal multiple-stage (MS) detector for the receiver that first translates the index bits using matched filtering, then translates the related data bits using two most likely estimates using a conventional ML approach. Modeling and arithmetic results demonstrate that the suggested design is superior to current SM and QSM based approaches, even if the MS methodology leverages FDA-based range and angle-dependent transmission to reduce the complexity of receiver processing. A high gain on-chip antenna for subterahertz applications could be made using silicon technology, according to research detailed in this journal. A 15-element array made up of circular and rectangular radiation patches is fed electromagnetic energy from a metal slot-line sandwiched between silicon and polycarbonate substrates using an aperture feeding mechanism. The location of this mechanism is above the polycarbonate layer. A microstrip line with an open end beneath the silicon substrate is orthogonal to the metal slot line. An open-ended microstrip line is stimulated to drive a metal slot line in order to link and output the signal from patch arrays. The on-chip antenna has an efficiency of 70.8 percent, which is below 10 dB at 0.290 to 0.316 terahertz, based on the results. The antenna's stopband, which is between 0.292 and 0.294 THz, is incredibly small. The antenna is 20 x 3.5 x 0.126 mm3 in size. We are looking at wireless energy transmission [25]–[27]. With a high base station antenna density, estimates from orthogonal and shared uplink pilot signaling systems enable Wireless Energy Transfer (WET) to a significant number of sensors. We obtain new upper bounds on the probability of a WET outage if each sensor node is unable to gather the minimum amount of energy Eu required to deliver uplink pilots and the energy Ep required for its primary operations. The base station antenna count increases as the number of sensor nodes, transmission power, channel estimate errors, and the type of pilot signaling technology employed increase. We demonstrate that the outage probability is the same with an orthogonal technique as it is with a shared strategy when the sensor nodes are equally distanced from the BS. When the two strategies are positioned at various angles to one another, the orthogonal strategy is more effective. To solve this problem, we offer a simple location-dependent clustering and hybrid pilot assignment method. The suggested method reveals an intriguing trade-off between outage performance and the resources required for channel estimation. Antenna arrays are widely used to locate active communication transmitters and passively reflected radar targets. Regrettably, since [8][15], localization quality has decreased. Temporal lags and incorrect antenna placement, especially in large array systems with many antennas spread out across a vast area These problems are brought on by cable phase instability and position misalignment unless the array is firmly in place. In-situ array calibration is required as a result. Inaccurate location may be caused by incoherent beacon signals. Multipath will have an effect on the in-situ calibration, causing the reference points of the array to be measured unevenly. In the near field, calibration is performed. The algorithm now runs significantly more fast as a result. Path losses could vary significantly owing to unknown causes.

The method used to produce effects that are physically convincing in a soundproofed setting, and the caliper is Results obtained indoors can be verified using three antennas. The paper mentions the calibration results of the arrays. This project aims to build a tiny MIMO antenna (MIMO). System for 5G terminal ground-radiation antennas. Little loop-shaped antennas radiate the earth. as portable radiators equipped with tiny, light-weight resonators that can excite the ground plane. For outdoor WLANs, its wind resistance is ideal. In this paper, a new biometric identifying trait for wearable communication applications is presented that blends physical layer properties with human body shape. Antenna-tissue interactions change the physical layer characteristics of tightly fitting wearable devices in a unique way. Return loss characteristics could be included into a cutting-edge biometric idea to identify people on different body areas. An upgraded directional coupler architecture and an improved antenna for identifying distinguishing features are used for human recognition. Classification accuracy was demonstrated to be more than 98 percent for stationary participants and greater than 93 percent for mobile participants using a prototype standalone test-bed with sensor circuits running at 2.45 GHz. Users can be validated and authorized using circuitry already found in wireless wearable communication systems as an indicator of return loss. Future wireless communications will benefit greatly from massive MIMO systems, which also have the potential to significantly boost ghostly proficiency. On the other hand, existing massive MIMO techniques use the conventional beamforming of phased arrays. Both expensive equipment and a lot of electricity are needed for this method. One of the leading technologies to enable intelligent and energy-efficient wireless roads has recently been recognized as the configurable intelligent surface (RIS), a two-dimensional structure with several passive components. This technique provides imaging systems with high gain, cheap cost, and great resolution. The suggested RIS combines stage shift and radioactive effects on an electromagnetic surface by using PIN diodes to offer 2-bit part shifting for beamforming. This innovative architecture led to the development of the first wireless statement model ever [20][25].

The prototype includes hosts for setting up parameters and exchanging data, Universal Software Radio Peripherals (USRPs) for baseband signal processing, and Receiver-Input-Output (RIO) for data transmission and receiving. Each of these components can be found in the prototype. Our findings show how effective and practical RISs are for wireless communications. The study's recommended RIS has a gain of 21.7 dBi at 2.3 GHz. At the millimeter wave frequency of 28.5 GHz, an antenna gain of 19.1 dBi is achieved (mmWave). The prototype for wireless communication based on RIS has also greatly reduced power consumption. PLS, which has drawn a lot of interest, provides vehicle networks with dependable and portable secure communications. Passive eavesdroppers are currently unprotected, even if they have multiple antennae. We propose a physical layer secure MIMO-SVD communication to close this gap. use a variety of antennas to thwart eavesdroppers (SSVD). SSVD-enhanced data frames are used at the transmitter to encrypt sensitive data. After that, the crucial data is attached to the wireless channel and broadcast along with integrated SSVD precoding, activated/non-activated MIMO parallel subchannels of the appropriate receiver, and the vital data.

Due to the exclusivity and independence of the wireless channel, only the authorized receiver is able to see the crucial information and utilize it to gradually decode (XOR) the secret data (bit error rate). Even with a large number of antennas, an eavesdropper will not be able to decipher any important information from the signals intercepted. Eavesdroppers are unable to "decrypt" any information pertaining to the confidential content because of the encryption. There have been offered conceptual and mathematical arguments for the validity of security and dependability. There are several chances to expand mobile capacity since the millimeter-wave (mmWave) frequency provides a wide bandwidth. mmWave propagation channels were measured and modelled between 2011 and 2013 using a wide-band descending correlator station with steerable turning horn probes at the transmitter and receiver. More than 15,000 influence postponement forms were generated by the mmWave bands, and these forms were utilized to develop path loss models, channel models, and outage probabilities. These models offer side-by-side comparisons of propagation quality across a variety of mmWave bands [12]–[18] for upcoming mmWave system expansion and calibration. Researchers may compare and standardize path loss parameters for creating mm/wave networks by applying these models of route loss in actual environments, including the use of directional projections.

Table 2.1: Performance Analysis of Microstrip Antennas

Frequencies(GHz)	Return Loss (dB)	Gain (dB)	VSWR	Efficiency (%)
2.5	-18.08	3.2	1.2	45
3.5	-20.28	4.2	1.4	55
4.5	-22.45	4.8	1.5	58
5.5	-25.98	5.2	1.4	65
6.5	-32.56	6.8	1.6	70
7.5	-30.85	7.2	1.8	75
8.5	-28.58	8.2	1.7	80

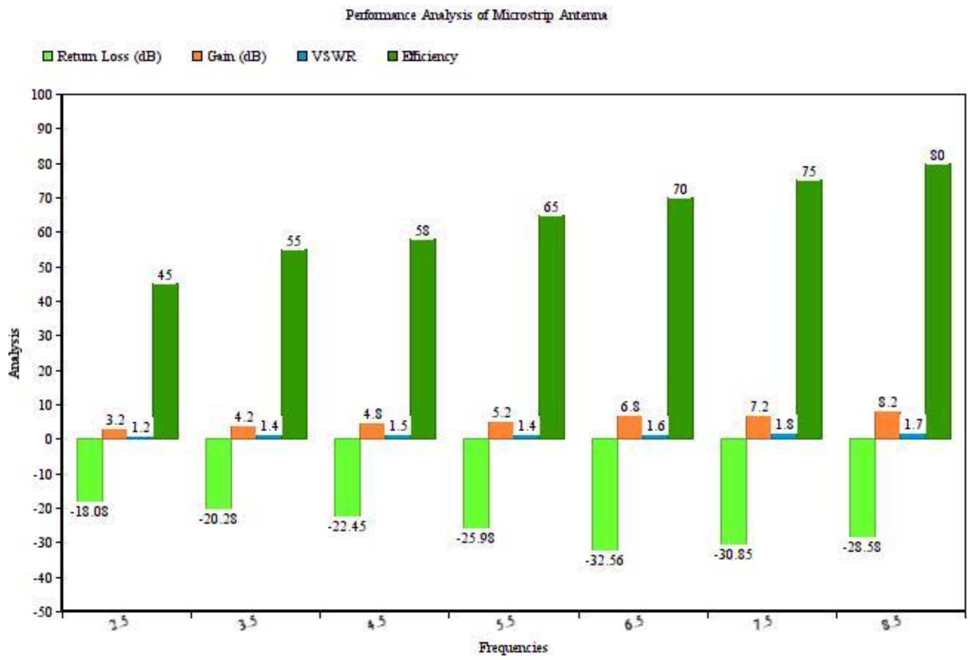

Figure 2.16: Performance Analysis of Microstrip Antennas

3.DISCUSSION OF THE METHODOLOGY

3.1 INTRODUCTION

Recently, microwave sensors invented the top ranks in the field of delegated sensing technology [1]. This is due to the fact, microwave radiations can penetrate through materials under test with excellent accuracy [2]. Nevertheless, most current microwave technologies lean on microstrip and printed circuitries; that can be embedded in highly compact integrated electronic devices [3]. The microwave sensors became attractive solutions for many biomedical issues because they have no ionization effects on the human body [4]. Nonetheless, they can operate at low energy conductions [5].

Microwave sensing is a proven tool for liquid characterization that has been used for more than decades [6]. Such sensing technology is based on measuring changes in scattering parameters (S-parameters) in relation to a sample under test (SUT) introduction [7]. The sensing evaluation can be transferred via a given algorithm to retrieve material characterizations at this step [8]. This can be quantized through field penetration as invasive or noninvasive technology.

Researchers involved metamaterials, closed-loop resonators, and other transmission line-based miniature microwave resonators for biomedical applications. The electromagnetic properties of these structures are affected by the frequency at which they operate. and how the consistency factor varies with different fluid introductions. Consequently, many researchers conducted their experimental studies to design novel microwave sensors with high accuracy for biomedical applications [6]. For example, in [7], a design of a printed interdigital capacitor was proposed for water pollution detection at 1.65GHz based on antenna design. Another design was proposed in [8] for blood grouse detection using a printed circuit antenna at 0.6GHz. In that design, the sensing technology was proposed based on touching the antenna terminal directly. Liquid profiles can be discussed by calculating S-parameters and complex dielectric properties. Any variation in those parameters can explain by a biological background. Most microwave biosensors operate by installing couplery thin tubes or slotted cylindrical tubes [9]. However, such technology adds extra losses on the quality of measurements [10]. Nevertheless, due to the problem of penetration into the skin, this technology has been found to be a very limited to many sensing processes [11].

Another application was in traduced in [12] for detection the moisture contents in crude oil derivatives using a microstrip fractal sensor. Later, another design was introduced in [13] to determine the quality of oil derivatives using electrical conductivity measurements at microwave frequencies. To measure the water content in the crude oil, the ultrashort wave technology was applied in [14]. A sensing method was proposed for measuring water content in crude oil using a high dielectric capacitor by measuring the phase angle conversion value in real-time process of water content in crude oil.

For future wireless communications, microwave and millimeter-wave technologies will coexist together to perform multi-band operations providing basic coverage for short-range high data rate connections [3]. Microwave filters based on microstrip lines are the most commonly used in microwave filter design for its advantages such as low cost, small size, and ease of fabrication. Many techniques have used for the design of multi-band filters such as the stepped-impedance microstrip resonators, multi-mode resonators, parallel coupled lines resonators and design by introducing transmission zeroes. Stepped-impedance resonators consist of two or more transmission lines with different characteristic impedances used for complexity reduction and miniaturizing the filter [4].

Recently, microwave sensors based composite right left hand (CRLH) structures were employed in the applications of biomedical systems for their pioneers properties [5]. For example, a single port measurement principle was introduced in [6] for dielectric properties characterizations. In [7], a probe sensor based on IDC structures was introduced for materials characterizations.

Medium, in the food safety and water pollution industry, many researchers have been attracted to microwave sensors because of their close relationship to people's lives and environmental environments [8]. Therefore, it is very important to determine the characteristics and components of food products [9]. Nowadays, many detection systems have been developed to determine the quality and properties of food products commonly used in daily life in a non-destructive manner [10]. Such a process makes it useful for sample monitoring with regard to both food safety and water system analysis [11]. The low-cost vector microwave system proposed in ref. [12] has the advantage over a single transmission line with improved sensitivity, allowing the volume and phase of the material under test to be measured. In [13], the fat and salt content of beef products are measured simultaneously using microwave technologies, which have advantages such as low cost, portability, and real-time operation. A high-resolution, resonance-based wireless microwave sensor was introduced to enable high-precision sensing in unreachable applications, while reducing battery usage [14]. The rapid development of mobile and wireless communication systems is increasing exponentially over the years, this leads to the requirements of designing filters that can operate with different cutoff frequencies in the same time. There are several techniques used for multi-band filter design, stub-loaded resonator [15], quarter-wave stepped impedance resonator [16], embedded resonator [17], meander split loop resonator [18], and substrate-integrated waveguide resonator [19]. For example, In [20] presented a novel dual-mode dual-band filters with independently controlled center frequencies and bandwidths using coplanar-waveguide-fed ring resonator using High Frequency Structure Simulator (HFSS) and the results have been verified practically. Two microstrip ring resonators were employed to obtain dual-mode dual-band responses. The ring resonators were fed simultaneously via novel feeding structure to conveniently control the coupling strength between resonators and feeding lines. The center frequencies were 1.4 GHz and 2.15 GHz with 10% and 3.3% fractional bandwidths. Researchers in [21] presented a novel dual-band bandpass filter with low insertion loss and high isolation between the passbands by introducing two symmetric stepped-impedance resonators and a pair of I/O ports. The filter was designed and fabricated on a 0.787mm thickness Duroid 5880 substrate with 2.2 dielectric constant achieving a compact side and high performance characteristics. The overall filter dimension was 30×21mm2 and this type of microwave filters can be applicable in the fields of global positioning system (GPS) and wireless local area network (WLAN). The two passbands were centered at 1.575 and 2.4 GHz respectively with isolation greater than 55 dB and fractional bandwidths for the two passbands of 6% and 3.8% respectively. [22] a dual-band bandpass filter has been designed using a multi-mode resonator for WLAN applications with Anosoft HFSS simulator. The bandwidth of the generated passbands can be controlled by adjusting the characteristic impedances and the four even/odd modes of the multi-mode resonator. The two passbands had transmission poles with high frequency selectivity and good harmonic suppression. The design have been implemented on a substrate (70mm×27mm) with dielectric constant of 2.65 and 0.5mm thickness. The first passband centered at 2.5 GHz and the second passband centered at 5.3 GHz with fractional bandwidths of 29.1% and 16.5% respectively. Good agreement between simulated and measured results has been achieved. In [23], the design of a dual-mode compact bandpass filter using a branch-loaded short-circuit gradient impedance resonator (SIR) and a branch-loaded short-circuit impedance resonator. The miniaturization technology was based on SIR hairpin geometry which can generate two resonance modes in two pass ranges while maintaining excellent performance. The structure consisted of two sets of resonators; resonator 1 was for the dual-mode dual-band hairpin SIR for generating the first and second passbands while resonator 2 was a short-circuited stub loaded resonator for generating the third passband. The center frequencies of the three passbands were located at 1.57 GHz (Global Positioning System GPS), 3.5 GHz (Worldwide Interoperability for Microwave Access WiMax), and 5.2 GHz (Wireless Local Area Network WLAN) with fractional bandwidths of 5.92%, 9.71%, and 5.5% respectively. The design was simulated using Anosoft HFSS on a substrate with a dielectric constant if 4.5 and 0.8mm thickness. The final circuit size was 15×13mm2. the authors in [24] proposed a compact microstrip bandpass filter for millimeter-wave applications. The filter consisted of 3-pole coupled-line modified hairpin resonator. The modification was to perform stepped-impedance resonator (SIR) on the hairpin lines to suppress the unwanted spurious harmonics, and to obtain transmission zero close to upper edge of the passband to increase the selectivity. The electrical length of the filter was approximately a half-wavelength at the mid-band frequency. The design has been performed by full-wave EM simulation on a RT/Duroid 6002 substrate with a dielectric constant of 2.94 and 0.129mm of thickness. The filter also has been fabricated experimentally with excellent agreement obtained. The center frequency was 34 GHz with very wide stopband with a rejection level better than 10 dB. The filter size was 2.45×1.46cm2. A compact ultra-wide band (UWB) millimeter-wave bandpass filter design was for proposed automotive radar systems in [25]. The filter consisted of two quarter-wavelength parallel-coupled line sections. A shunt ring resonator and a shunt stepped-impedance open-circuited stub were loaded at the center between the parallel-coupled lines to produce transmission zeroes at each side of the passband and increase the selectivity. The filter design was realized on RT/duroid 6002 substrate with dielectric constant of 2.94 and 0.127mm thickness. The filter was realized by EM simulation and also was verified practically with good agreement between simulated and measured results. The UWB spectrum obtained was ranging from (22-29 GHz) centered at 25.5 GHz with less than 3.7 dB insertion loss at the mid-band frequency and 22% fractional bandwidth. In [26] anticipated a dual-band bandpass filter with independent control of the center frequencies and with wide stopband suppuration. This filter was designed by using a new quintuple-mode resonator (QMR). The analysis of the frequencies was done by using odd and even modes methods and showed that five modes can be achieved. The first two modes were used for the design of the lower passband, while the other three modes were used to attain the higher passband. The filter was fabricated on a Rogers 4003C substrate with 0.508mm thickness and dielectric constant of 3.55. Compact size and tunable passbands were achieved. The passband frequencies centered at 2.96 and 5.695 GHz with fractional bandwidths of 27.7% and 23.4% respectively. A new idea for combining microwave-band with millimeter-waveband in one filter was proposed in [27]. The proposed filter operated at dual-/tri-band frequencies. A microwave BPF with wide stopband up to millimeter-waveband was implemented based on stepped-impedance resonator principles and low-pass filter. The design technique based on aperture coupling mechanism. The filter consisted of three parts, first part was a low-pass filter for obtaining the microwave-band frequency, the second part was a stepped-impedance resonated based filter for ultra-wide stopband up to millimeter wave region, and substrate-integrated waveguide based filter was used to obtain the millimeter-wave frequency. The filter designed on three sections of RT/duroid 5880 dielectric substrates of 2.2 dielectric constant and 0.508mm thickness and conducting materials. The simulation was performed using full-wave HFSS, and the filter also fabricated practically with good agreement between simulated and measurement results. The cut-off frequencies obtained were centered at 2.4 and 30 GHz. This dual-band filter was also modified for a tri-band operation by some adjustments on the design to give a third cutoff centered at 5.2 GHz. The proposed filter can be used at antennas, power amplifiers, low-noise amplifiers, and so on. A tri-wideband bandpass filter (TWB-BPF). The filter distinguished with a compact size, high isolation between the passbands, and multiple transmission zeros (TZs) was proposed in [27]. The design was established on the principles of the multiple-mode resonator (MMR), with using odd/even modes analysis. Ten TZs were obtained to enhance the band-to-band isolation and widen the stopband suppression. The TWB-BPF was fabricated on a Rogers 4003 substrate with a thickness of 0.508 mm and 3.38 dielectric constant. The oprating frequencies were centered at 1.07, 3.25, and 8.32 GHz with fractional bandwidths of 37.4%, 43.5%, and 40.4% respectively. Good agreement were obtained between simulated and measured result.

It is good to mention, the previous survey focused on two parts, the first part was concerning the design of dual/multi-band BPFs at microwave bands mostly by using stepped-impedance resonator theory for good out-of-band rejection and compact size, while the second part concerned about the design of millimeter-wave bands BPFs. There is a lack of researches which investigate designing dual-band filters that can operate at microwave and millimeter-wave bands simultaneously. This work will illustrate the design of multi-band BPF at microwave band, and dual-band BPF at microwave and millimeter-wave bands.

In this work, Se Suggests a highly sensitive microwave blood monitoring system using CSI. The system is designed to run around 4.46GHz and is easy to integrate with other platforms. Through careful experimentation and analysis, the proposed sensor has the ability to identify common blood and determine the variation in resonators. This sensor provides excellent response with materials subject to changes in test properties. For this, the nonlinear effects are eliminated significantly by asymptotic the insertion loss changes to linear variations. Thus, the measurements accuracy is increased rapidly in comparison to the relative published designs. To prevent the distortion effects, the suggested sensor performance is managed by an LDR component with a back loop topology. The advantages of the suggested system include inexpensive manufacturing and measurement costs, a straightforward design, simple operation, measurement accuracy, a very low sample consumption, and high sensitivity, which makes the system appealing for sensing applications.

3.2 SENSOR DESIGN AND DETAILS

The suggested sensor design's specifics and related geometric dimensions are covered in this section. as the image depicts. The proposed sensor has three major components, as shown in Figure 3.1 (a): The first component uses a standard transmission line that is zigzaggedly charged by an interdigital capacitor. The meander is regarded as the second phase, in which the conductive effect is changed to create a massive, elegantly chaotic state. The third component is introduced as a five-finger interdigital capacitor. Combining several capacitor inductor branches will improve the quality factor, which is the fundamental benefit of linking these structures together. [3]. Thus, the authors developed the transmission line model based on employing an analogous circuit model of lumped elements, as seen in Fig. 3.1, to realize the effects of these parts (b). The primary three components of the suggested sensor are essentially described by the derived circuit model. Models for the transmission line's LT, CT, RT, and GT lengths are used. The transmission line losses in that form are modeled as conductor and dielectric losses from the conductive layers and the substrate layer [4]; these losses are denoted as RT.L and GT.L, respectivelyThe magnetic field created by the surface current motion on the conductive traces is then perpendicular to the current motion [9]; this magnetic field can then be stored in the inductive component (LT.L) of the transmission line [7]. The stored electrical field energy [8] in the substrate to be given as CT.L describes the trapped electrical field that exists between the patch and the ground plane layer.

The consequences of the meander line are then explained by the (CM, LM, RM) parallel branch. The consequences of resonance energy storing bandwidth are depicted in this figure [10]. Due to the consequences of size reduction, such stored energy is characterized by maximizing the quality factor in the suggested meander line and lengthening the electrical channel in the downsized area [11]. This acknowledges the reality that lowering radiation losses actually raises quality factors [12]. The inductive and capacitive effects produced by this approach are provided by the LM and CM, respectively. RM provides the implications of the radiation losses from the suggested meander line. The (Cidc, Lidc, and Ridc) parallel branch provides the effects of adding the interdigital capacitor. This branch is created by joining the fingers that, as Cidc and Lidc, respectively, store the electric field inside and the current motion on the conductive trace. The Ridc value of the same branch is used to describe the coupling resistance's effects. The actions of the voltage gradient inside the air space between the fingers are what cause this coupling [15]. In order to maximize the load matching between the [6], the coupling between the meander line and the interdigital capacitor is defined using CC. Table I contains a list of the suggested circuit model's relative values.

To achieve the distortion-less requirement according to equation (3.1) from [12], a stub connection is introduced at the junction between the interdigital capacitor and the inductor.

$$\frac{R}{L} = \frac{G}{C} \tag{3.1}$$

where, R is the equivalent conduction loss of SUT, G is the equivalent dielectric loss of SUT, L and C are the effective permeability and permittivity of SUT, respectively. As maintained later, the proposed sensor is constructed from an interdigital capacitor to remove the effects of the imaginary component that is generated by the indictor structure which mainly stores the energy from the propagation [13]. The inductor structure is invoked to be a spiral geometry cause of being a highly sensitive stricter that concentrate the current before being transferred to SUT.

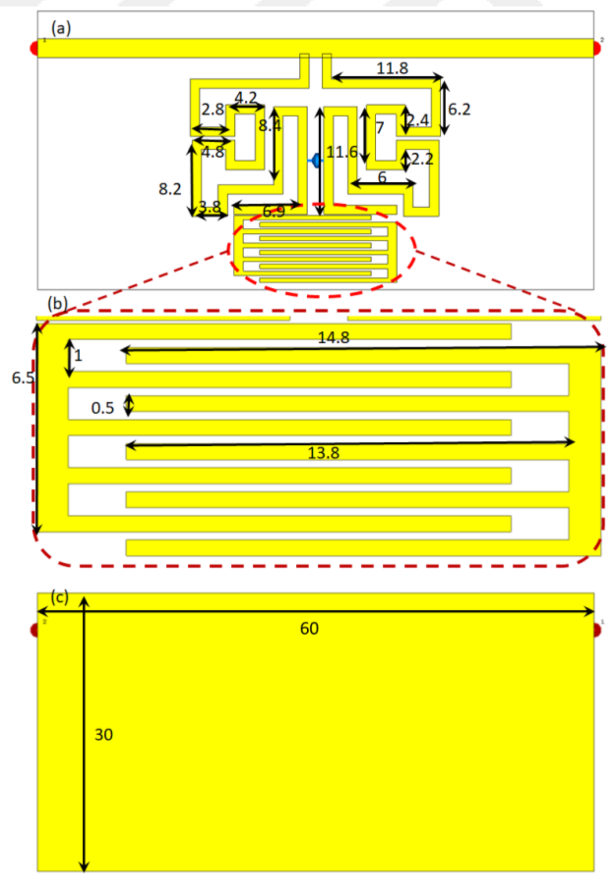

Figure 3.1: The proposed sensor geometry: (a) full structure, (b) IDC, and (c) back view. Note: all dimensions are in mm scale.

3.3 DESIGN METHODOLOGY BASED CIRCUIT ANALYSIS

The proposed CSI design, see Figure 3.2, parameters basically are: The line width is 0.5 mm, space between turns is 0.5 mm, number of turns is considered 6, the outer diameter is fixed to 6.5 mm, and inner diameter is 1mm. Figure 2 shows the transmission lumped element model of the proposed resonator. Since, the current motion is trapped in the conductive traces [14]. The authors assumed their equivalent circuit model is a series branch of inductive and resistive losses of (L_s) and (R_s), respectively, in parallel with a spacing capacitor (C_s) [15]. This explains the physical meaning of the quality factor of the circuit by having the ratio between the stored and the dissipated energy [15]. Such phenomena can be expressed as the following:

$$Q = \frac{\omega Ls}{Rs} \cdot \frac{1}{1+\frac{Rs}{Rp}\left[\left(\frac{\omega Ls}{Rs}\right)+1\right]} \cdot \left[1-\frac{Rs^2(Cs+Cp)}{Ls}-\omega^2 Ls(Cs+Cp)\right] \tag{3.2}$$

where ω is the radian frequency and RP is the parasitic resistance. The total effective RS by taking into account the phenomenon of eddy current [16], can be obtained as:

$$Rs = \frac{\rho l}{W\delta\left[1-e^{-\frac{t}{\delta}}\right]} \tag{3.3}$$

where δ, is the skin depth, ρ is the conductivity of the metal used in inductor, l and t are the length and thickness of the inductor, respectively.

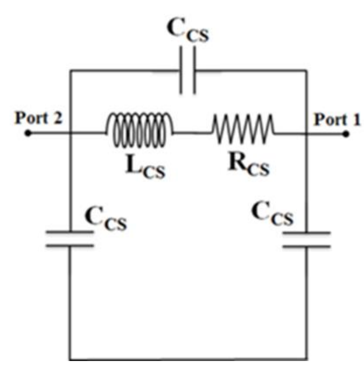

Figure 3.2: The proposed CSI structure: (a) CSI numerical model and (b) equivalent circuit model.

Using CST MWS, the sensor is designed to provide frequency resonance variation with liquid sample presence. The proposed IDC structure, see Figure 3.3(a), is considered to miniaturize the effective sensor size and enabling the normal electrical field component in the field intensity through increasing the inherent permittivity of the structure [17]. The benefit of IDC compared to other resonance structures (e.g., SRR) is to provide multiple resonances with relatively high quality factors [18]. The interdigital capacitor is a periodic multi-finger structure that can be used as a sequential capacitor in planar transmission lines [19]. In Fig. 3.3(b), the proposed IDC is represented by the proportional equivalent circuit model. Typically, the amplitude of these structures ranges from 0.05 pF to about 0.5 pF and can be increased by increasing the number of fingers or by adding a thin layer of high dielectric constant material between the conductors and the substrate [19]. String capacitance for each IDC length with physical parameter:

$$C_{int} = \frac{\varepsilon_r + 1}{W_{int}} L_{int}[(N-3)A_1 + A_2] \quad (3.4)$$

$$A_1 = 4.41 \tanh\left[0.55\left(\frac{h}{w}\right)^{0.45}\right].10^{-6}(pF/\mu m) \quad (3.4.A1)$$

$$A_2 = 9.92 \tanh\left[0.52\left(\frac{h}{w}\right)^{0.5}\right].10^{-6}(pF/\mu m) \quad (3.4.A2)$$

where εr is the substrate permittivity, N is the number of structure fingers and the dimensions Wint and Lint are the finger width and length, respectively, [19]. For the parameter h is the substrate thickness and w is the width of one finger.

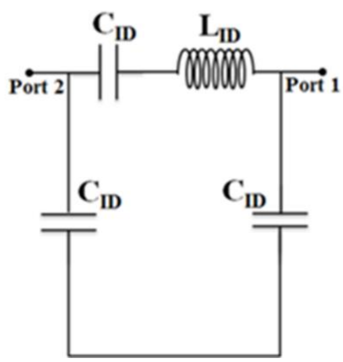

Figure 3.3: The proposed IDC structure: (a) IDC numerical model and (b) equivalent circuit model.

Now, in the proposed design, the Hilbert-curve shape has been investigated in order to reduce the proposed sensor size and increase the frequency resonances [15]. The considered fractal geometry is based on the 3rd order Hilbert geometry as seen Figure 3.4(a). The proposed Hilbert geometry equivalent circuit model, see Figure 3.4(b), is derived based on Richard Koch theory [19].

Based on the simulation results, As shown in Fig. 3.4, the equivalent circuit model of the proposed unit cell is derived (b). Equivalent coupling capacitances between the unit cell and adjacent cells are referred to as the left capacitor (CST) and the fractal slot is considered as an inductor (LST) where the movement of magnetic current can be amplified in air traces. [12]. This inductor is equivalent to the magnetic field stored within the fractal grooves of the rings [6]. The material loss is determined by the resistance to RST [12].

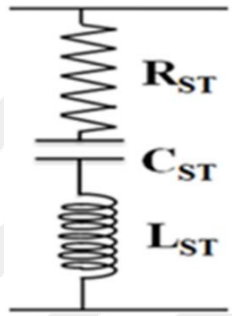

Figure 3.4: The proposed Hilbert structure: (a) Hilbert numerical model and (b) equivalent circuit model.

The proposed sensor design is conjugated with a back loop structure. The advantage of such introduction is to realize a band reject filter response instead of having a passband resonance. Such change increases the results accuracy during the measurements [20]. Therefore, the back loop design is equivalently modeled as a PIN diode with an equivalent circuit that is shown in Figure 3.5.

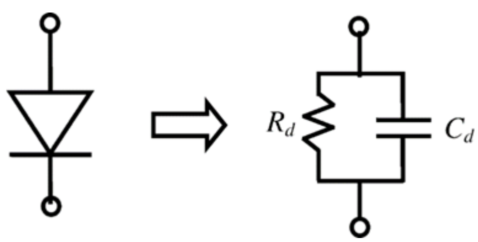

Figure 3.5: The proposed circuit model of the proposed back loop structure.

Lastly, the similar circuit model based on the developed RLC network, which is typically built as an IDC in series connection with a CSI and the Hilbert fractal, is used to analytically deduce the proposed sensor design based on an equivalent circuit model. The lumped elements Richard model [10] is used to create the suggested structure equivalent circuit model. As shown in Figure 3.6, the suggested circuit model is constructed by coupling a 50 input impedance RF source in series with a (R-L-C) parallel branch. An inductive segment LT and capacitive air gaps Cgap, which were previously shown in Figure 3.6, set apart the primary transmission line. Examining and contrasting the suggested circuit model S-parameters with those obtained using CST MWS. According to the mentioned lumped parts, which are modelled in Advanced Devices Simulator (ADS). The evaluated RLC components are listed in Table 3.1.

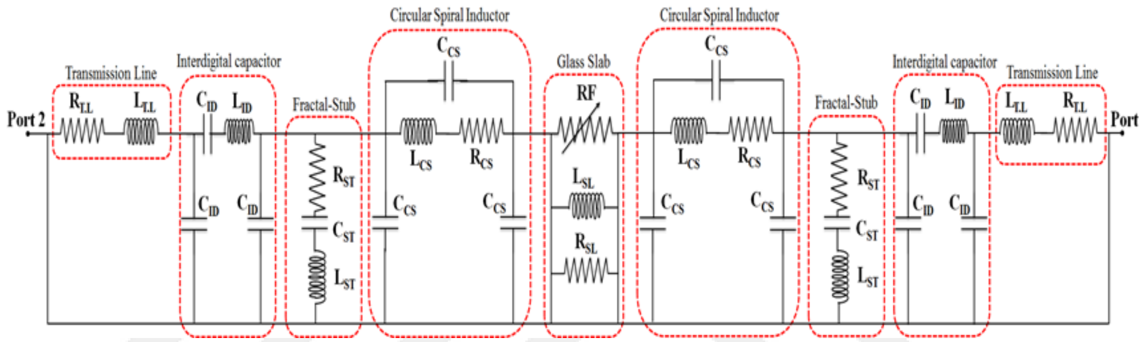

Figure 3.6: The proposed circuit model of the proposed sensor structure.

Table 3.1: Lamped element values of the equivalent circuit model in figure 3.6.

Element	Value
Resistance of the left hand (RLH)	12.2 Ω
Resistance of the right hand (RRH)	50 Ω
Conductance of the left hand (GLH)	0.1 S
Conductance of the right hand (GRH)	4 S
Capacitance of the left hand (CLH)	1.1pF
Capacitance of the right hand (CRH)	3.1pF
Inductance of the left hand (LLH)	3nH
Inductance of the right hand (LRH)	2.2nH

4.SENSING METHODOLOGY AND NUMERICAL RESULTS

The proposed sensor design is mounted under a light source directly on top of the human finger. The position of the sensor is located under the finger to collect the transmitted light at LDR port. Therefore, when the resistance level is changed, simultaneously of the output voltage is changed. In such variation, the output voltage is changed significantly to give an indication of glucose level variation. As seen in Fig. 4.1, the sensing methodology is shown to explain the sensing methodology.

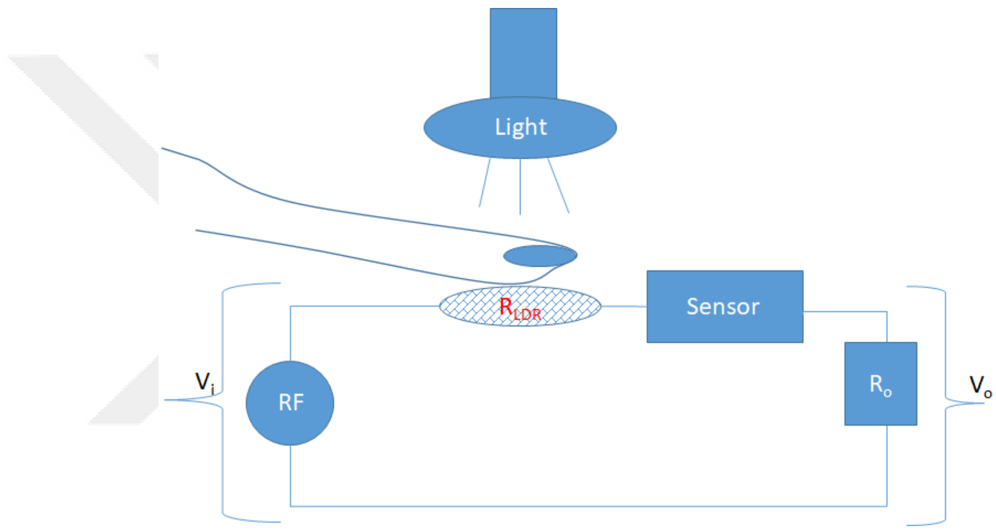

Figure 4.1: The simplified block diagram of the design based on reconfigurable technology.

The proposed work of this section is conducted based on generating an output voltage from the proposed sensor design. On top of that, the main limitation in the discussed work in the previous chapter is the difficulty of linearizing the measurements that generate a severe discrepancy in the detection accuracy. The main reason for such a discrepancy is the effects of the field fringing from the boundary conductions between layer discontinuities. Nonetheless, industrially, measuring the moisture contents in fluids like Blood, usually, is realized by the voltage level change on an output resistor of an electronic system. Such a process increases the compatibility of sensors with the microprocessors which is more recognizable with an easy manner than considering S21 Spectrum measurements. Also, laying on measuring the moisture content variation in the crude oil based on the frequency shift acquires an RF source to generate more than a frequency band to trac the frequency variation from the sensor with respect to SUT introduction. Thus, the system complexity could be increased with the effective cost. Therefore, it is subject of this research to conduct a novel the use of a photoresistors to control the proposed sensor performance with respect to SUT introduction. In such a technique, we eliminated the effects of the field fringing from different layers discontinuity. Moreover, the measured output voltage is induced by a RF rectifier at the output port of the sensor, as shown in Figure 4.1. It is good to mention that the proposed sensor is connected to a varactor diode to control the frequency of operation for a particular SUT when the caution calls. In this way, a back loop feed is proposed based on a varying capacitor. Therefore, the advantage of including that is to control the charging rise time till the photoresistors reaches the saturation, in which case the variation of the group velocity would be minimized and for that the nonlinearity of the measurements would be eliminated significantly.

In this section, the measurement results of the proposed sensor are discussed in details. As mentioned previously, firstly a neural network was applied in the previse chapter to predict the complicated nonlinear responses relationships by combining a permittivity measurements with water content. Now, in this chapter, the use of a reconfigurable technology based on photoresistors to detect the variations through controlling the resistive part only of the proposed sensor with respect to the SUT introduction. In such technique, the capacitive and/ or inductive parts of the proposed sensor would not be affected; that realizes a frequency resonance stability. Nevertheless, the nonlinear effects due to the energy fringing during the measurement process from the boundary discontinuities at SUT layers, pans, and sensor parts would eliminated. To achieve that, the performance of the proposed sensor is reconfigured with two photoresistors. Next, two capacitors are included to the design to perform several functions such as: For tuning the sensing resonance at the desired frequency band, increasing the measurement accuracy by controlling the feedback accumulation process, and reducing the phase velocity to be comparable to the group velocity during the measurements that minimize the distortion effects. In such advantages, the time delay that is required to achieve the accurate results would not be affected by the slow response of the photoresistors that need time for capacitor charging process. Also, the proposed measurement technique uses the light intensity to detect the characteristics of SUT; in such method, SUT transparency would be the dominate property for detection with fixing the incident light intensity on the photoresistors. Therefore, the incident light would carry the material properties and reflect that on the resistance value of the photoresistors. It is well known, that liquids transparency is an excellent criteria for their properties recognizing. Nevertheless, the light wavelength is very comparable to the liquids molecules size. With such aspects, we proposed this study for moisture content detection. This measurement technique is invoked by conducting the same measured samples with the neural network technique to compare the relative errors from each other.

We introduced the use of LDR optical switch to the propose design to applied resistive effects on the propose sensor. Such effects would maintain the frequency resonance at the same location without effective frequency difference [17]. Therefore, the main effects of LRD variation could happen from varying the insertion loss magnitude. Such variation effects significantly on the output voltage with linear response. There for the relative issues of diffraction from multiple layers could be reduce significantly [17].

Now, to explain the effects of changing R_{LDR} resistive part only propose sensor performance mathematical derivation is expressed in equation based on voltage divider role as following:

$$R_{LDR} = 26\text{K}\Omega^{-0.85IoT} \tag{4.1}$$

$$T = Ae^{-1.6\times10^{-2D}} \tag{4.2}$$

$$R_{LDR} = 26\text{K}\Omega e^{-0.85Ioe^{-1.6\times10^{-2D}}} \tag{4.3}$$

$$S_{12} = \frac{Vo}{Vin} = \frac{Ro}{Ro+R_{LDR}} \tag{4.4}$$

where, Io is the light intensity from the source, A is the area of sample, D is the glucose level, T is the transparency, R_{LDR} is the resistance of the LDR, Ro is the output resistance, V_o is the output voltage, and V_{in} is the input voltage[7][9].

4.1 SENSOR OPERATION AND RECONFIGURATION PROCESS

The authors proposed in this section, the operation and reconfiguration scenarios that are developed to visualize the conducted approach to understand the sensor operation. By varying the resistance of the introduced LDR value from 100Ω to 1000Ω, a significant variation in the proposed sensor S_{21} spectra is achieved as seen in Figure 4.2. Such variation is attributed to the effects of the voltage division between the total impedance of the proposed sensor and the LDR [21]. For this, the current motion would be significantly affected and pass through the back loop structure to be dissipated in the proposed fractal geometry. Therefore, such dissipation would be very useful for sensing as will be seen later. In Figure 7,the frequency resonances are found at, 1.22GHz, that all would be applied in the sensing process of this work.

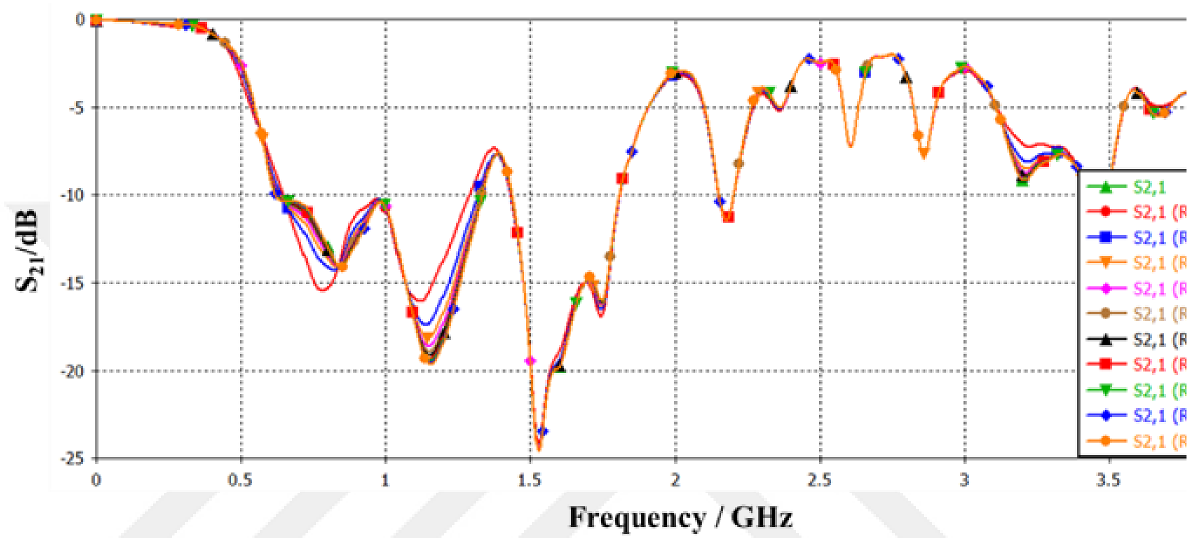

Figure 4.2: Evaluated S_{21} spectra with respect to varying the LDR value.

4.2 EXPERIMETAL VALIDATIONS

The proposed sensor is created and numerically evaluated as shown in Figure 4.3. (a). A chemical etching procedure is used to create the suggested sensor. Using an Agilent vector network analyzer, the proposed sensor's S21 spectra are analyzed before and after blood is introduced on top of the LDR spot. The obtained results before and after Blood introduction are presented in Figure 4.3(b).

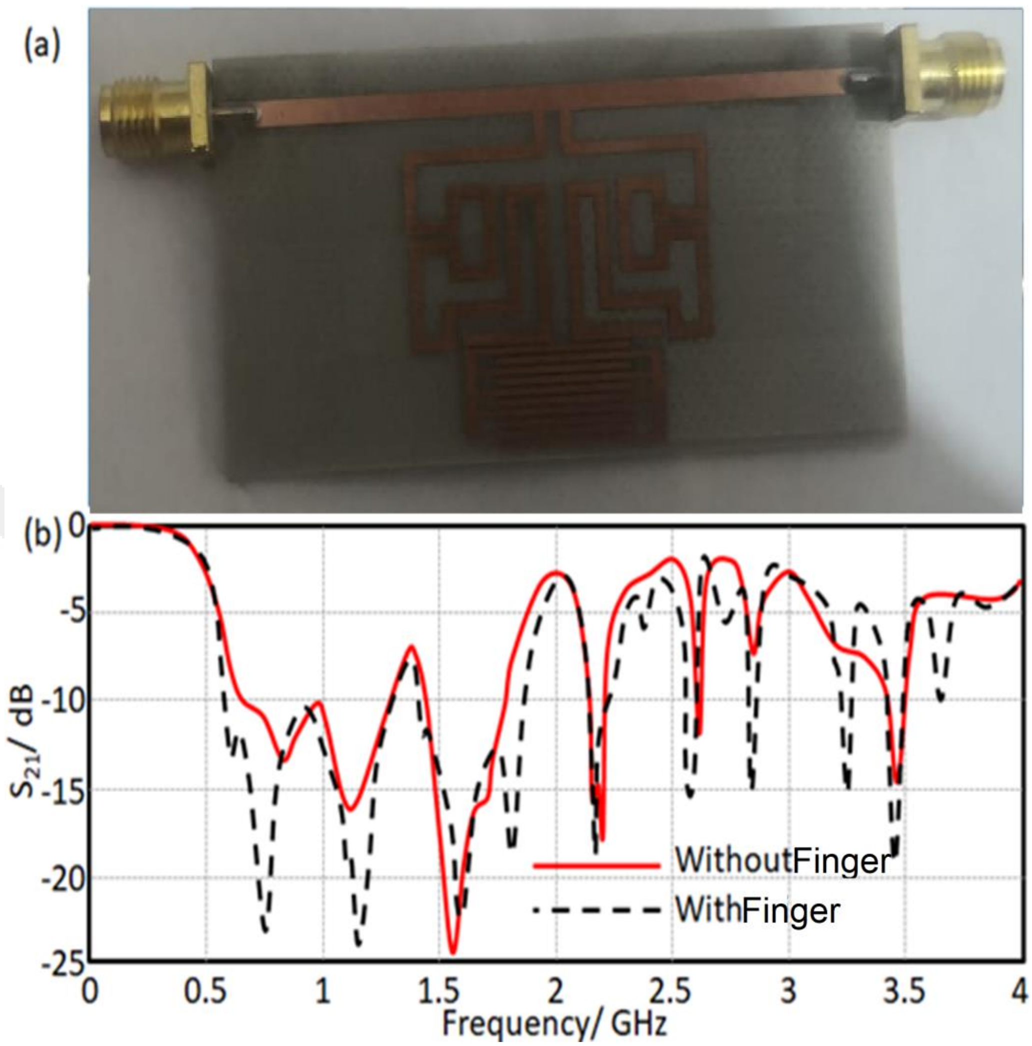

Figure 4.3: Experimental part: (a) fabricated sensor prototype and (b) S_{21} spectra.

The authors used an experimental investigation to test the impact of glucose level variation on the sensor performance at 1.22GHz, as listed in Table 4.1, to validate the efficacy of such methods. The instances in the list are evaluated based on their blood colors, which range from normal to severely dehydrated. These cases are taken into consideration in accordance with [13]'s medical guidelines. The results show that the suggested sensor is a superb choice for measuring glucose and may hold great promise for other biological fluid characterizations.

Table 4.1: Measured glucose influence in the proposed sensor performance.

Glucose level	**S_{21}**
150	-11.8
130	-13.2
210	-14.9
290	-17.5
390	-20.1
470	-24.8
550	-27.7

5.CONCLUSION AND FUTURE WORKS

5.1 CONCLUSION

Blood from 11 patients is used as the test material for the proposed sensor during fabrication and testing. The operating approach is essentially a novel use of an LDR component that realizes a linear change in the sensor performance with variations in blood glucose. The reason for these variations is thought to be a change in the transparency of the blood being tested, which affects the frequency shift and S21 magnitude. The ratio in the S21 magnitude is determined to be extremely substantial at 1.22GHz with linear change, according to the scientists. Due to the consequences of linear variation, the authors were motivated by this fact to think that their unique design would make a great candidate for sensing. The impacts of introducing the suggested sensor elements are investigated using the proposed sensor circuit model. Each component is implemented through a circuit branch, and the generated results from the numerical results are contrasted with them. Excellent agreements are found when those results are compared to the measured results.

5.2 FUTURE WORKS

a. In future work, it is planned to use the proposed sensor on a flexible substrate for wearable biomedical devices due to its snowballing demands in the trade. Therefore, we plan to test this device with different biological solutions.

b. Apply these measurements to the biological fluids using the same proposed technology. This technology based photoresistors is found to be more applicable to the variation measurements in the biological fluids where the light wavelength is very comparable to the molecule size.

c. The use of different fractal geometries is one of the scope of this work. Therefore, the author is planning to conduct other types of fractal to increase the electric felid fringing at the frequency band of interest.

d. The proposed sensor is constructed from a transmission line without applying the use of interdigital capacitors or stub via; that could increase the sensing quality and size reduction.

e. Connect the relative part of RF harvesting measurements, to a neural network based on fuzzy algorithm, to indicate the real values of particular responses whether in the biological or industrial instrumentation process.

REFERENCES

[1] C. Caloz and T. Itoh, *Electromagnetic Metamaterials: Transmission Line Theory and Microwave Applications: The Engineering Approach*. 2005.

[2] A. Nieuwoudt and Y. Massoud, “Optimizing the design of tunable spiral inductors for on-chip wireless applications,” *IEEE Wirel. Microw. Technol. Conf. WAMICON 2006*, no. 1, pp. 1–5, 2006, doi: 10.1109/WAMICON.2006.351926.

[3] S. R. Best, “A comparison of the resonant properties of small space-filling fractal antennas,” *IEEE Antennas Wirel. Propag. Lett.*, vol. 2, pp. 197–200, 2003, doi: 10.1109/LAWP.2003.819680.

[4] I. Bulu and H. Caglayan, “Designing Materials With Desired,” *Microw. Opt.*, vol. 48, no. 12, pp. 2611–2615, 2006, doi: 10.1002/mop.

[5] S. Gruszczynski, R. Smolarz, and K. Wincza, “Realization of high-performance broadband quadrature directional couplers in UMS PH25 technology,” *Electron.*, vol. 8, no. 12, 2019, doi: 10.3390/electronics8121520.

[6] S. Hardinata, F. Deshours, G. Alquié, H. Kokabi, and F. Koskas, “Biosensor miniaturization for non-invasive measurements of materials and biological tissues,” *Proc. - 2017 Int. Semin. Sensor, Instrumentation, Meas. Metrol. Innov. Adv. Compet. Nation, ISSIMM 2017*, vol. 2017-January, pp. 137–140, 2017, doi: 10.1109/ISSIMM.2017.8124278.

[7] W. Liu, H. Sun, and L. Xu, “A microwave method for dielectric characterization measurement of small liquids using a metamaterial-based sensor,” *Sensors (Switzerland)*, vol. 18, no. 5, 2018, doi: 10.3390/s18051438.

[8] H. Hao, D. Wang, Z. Wang, B. Yin, and W. Ruan, “Design of a high sensitivity microwave sensor for liquid dielectric constant measurement,” *Sensors (Switzerland)*, vol. 20, no. 19, pp. 1–14, 2020, doi: 10.3390/s20195598.

[9] Z. Wei *et al.*, “A high-sensitivity microfluidic sensor based on a substrate integrated

waveguide re-entrant cavity for complex permittivity measurement of liquids," *Sensors (Switzerland)*, vol. 18, no. 11, 2018, doi: 10.3390/s18114005.

[10] S. Liao, B. Gao, L. Tong, X. Yang, Y. Li, and M. Li, "Measuring complex permittivity of soils by waveguide transmission/reflection method," *Int. Geosci. Remote Sens. Symp.*, vol. 2019-July, pp. 7144–7147, 2019, doi: 10.1109/IGARSS.2019.8900535.

[11] J. G. D. Oliveira, E. N. M. G. Pinto, V. P. S. Neto, and A. G. D'assunção, "CSRR-based microwave sensor for dielectric materials characterization applied to soil water content determination," *Sensors (Switzerland)*, vol. 20, no. 1, 2020, doi: 10.3390/s20010255.

[12] M. G. Mayani, F. J. Herraiz-Martinez, J. M. Domingo, and R. Giannetti, "Resonator-Based Microwave Metamaterial Sensors for Instrumentation: Survey, Classification, and Performance Comparison," *IEEE Trans. Instrum. Meas.*, vol. 70, 2021, doi: 10.1109/TIM.2020.3040484.

[13] A. L. McKenzie and L. E. Armstrong, "Monitoring Body Water Balance in Pregnant and Nursing Women: The Validity of Urine Color," *Ann. Nutr. Metab.*, vol. 70, no. Suppl1, pp. 18–22, 2017, doi: 10.1159/000462999.

[14] L. E. Armstrong, M. S. Ganio, J. F. Klau, E. C. Johnson, D. J. Casa, and C. M. Maresh, "Novel hydration assessment techniques employing thirst and a water intake challenge in healthy men," *Appl. Physiol. Nutr. Metab.*, vol. 39, no. 2, pp. 138–144, 2014, doi: 10.1139/apnm-2012-0369.

[15] A. Ebrahimi, J. Scott, and K. Ghorbani, "Differential sensors using microstrip lines loaded with two split-ring resonators," *IEEE Sens. J.*, vol. 18, no. 14, pp. 5786–5793, 2018, doi: 10.1109/JSEN.2018.2840691.

[16] L. Su, J. Naqui, J. Mata-Contreras, and F. Martin, "Modeling and Applications of Metamaterial Transmission Lines Loaded with Pairs of Coupled Complementary Split-Ring Resonators (CSRRs)," *IEEE Antennas Wirel. Propag. Lett.*, vol. 15, pp.

154–157, 2016, doi: 10.1109/LAWP.2015.2435656.

[17] H. Y. Gan *et al.*, "Differential Microwave Microfluidic Sensor Based on Microstrip Complementary Split-Ring Resonator (MCSRR) Structure," *IEEE Sens. J.*, vol. 20, no. 11, pp. 5876–5884, 2020, doi: 10.1109/JSEN.2020.2973196.

[18] R. K. Abdulsattar, T. A. Elwi, and Z. A. Abdul Hassain, "A new microwave sensor based on the moore fractal structure to detect water content in crude oil," *Sensors*, vol. 21, no. 21, pp. 1–18, 2021, doi: 10.3390/s21217143.

[19] T. Haq, C. Ruan, S. Ullah, and A. Kosar Fahad, "Dual notch microwave sensors based on complementary metamaterial resonators," *IEEE Access*, vol. 7, pp. 153489–153498, 2019, doi: 10.1109/ACCESS.2019.2948868.

[20] A. A. Al-Behadili, I. A. Mocanu, T. M. Petrescu, and T. A. Elwi, "Differential microstrip sensor for complex permittivity characterization of organic fluid mixtures," *Sensors*, vol. 21, no. 23, pp. 1–20, 2021, doi: 10.3390/s21237865.

[21] R. K. Abdulsattar, T. A. Elwi, and Z. A. A. Hassain, "Microwave Resonator based a Fractal Moore Structure for Modern Wireless Reconfigurable Systems," *ICRACOS 2021 - 2021 3rd Int. Conf. Res. Acad. Community Serv. Sustain. Innov. Res. Community Serv. Better Qual. Life Towar. Soc. 5*, pp. 98–102, 2021, doi: 10.1109/ICRACOS53680.2021.9701943.

[22] M. Saadat-Safa, V. Nayyeri, M. Khanjarian, M. Soleimani, and O. M. Ramahi, "A CSRR-Based Sensor for Full Characterization of Magneto-Dielectric Materials," *IEEE Trans. Microw. Theory Tech.*, vol. 67, no. 2, pp. 806–814, 2019, doi: 10.1109/TMTT.2018.2882826.

[23] X. Zhang, C. Ruan, T. Ul Haq, and K. Chen, "High-sensitivity microwave sensor for liquid characterization using a complementary circular spiral resonator," *Sensors (Switzerland)*, vol. 19, no. 4, 2019, doi: 10.3390/s19040787.

[24] N. K. Tiwari, S. P. Singh, and M. J. Akhtar, "Novel Improved sensitivity planar microwave probe for adulteration detection in edible oils," *IEEE Microw. Wirel.*

Components Lett., vol. 29, no. 2, pp. 164–166, 2019, doi: 10.1109/LMWC.2018.2886062.

[25] L. Su, J. Mata-Contreras, P. Vélez, A. Fernández-Prieto, and F. Martín, “Analytical method to estimate the complex permittivity of oil samples,” *Sensors (Switzerland)*, vol. 18, no. 4, pp. 1–12, 2018, doi: 10.3390/s18040984.

[26] C. Sen Lee and C. L. Yang, “Thickness and permittivity measurement in multi-layered dielectric structures using complementary split-ring resonators,” *IEEE Sens. J.*, vol. 14, no. 3, pp. 695–700, 2014, doi: 10.1109/JSEN.2013.2285918.

[27] C. S. R. Csrrs, L. Su, J. Naqui, J. Mata-contreras, and F. Martín, “Modeling and Applications of Metamaterial Transmission Lines Loaded With Pairs of Coupled,” vol. 15, pp. 154–157, 2016.